



1 **Estimation of Long-term Gridded Cloud Radiative**
2 **Kernel and Radiative Effects Based on Cloud Fraction**

3 Xinyan Liu¹, Tao He^{*2}, Qingxin Wang³, Xiongxin Xiao⁴, Yichuan Ma⁵, Yanyan
4 Wang¹, Shanjun Luo¹, Lei Du¹, Zhaocong Wu^{1,2}

5 ¹ Aerospace Information Research Institute, Henan Academy of Sciences, Henan 450046, China

6 ² Hubei Key Laboratory of Quantitative Remote Sensing of Land and Atmosphere, School of Remote
7 Sensing and Information Engineering, Wuhan University, Wuhan 430079, China

8 ³ College of Geography and Environmental Sciences, Zhejiang Normal University, Jinhua 321004,
9 China

10 ⁴ Institute of Geography and Oeschger Center for Climate Change Research, University of Bern, Bern
11 3012, Switzerland

12 ⁵ Department of Geography, The University of Hong Kong, Hong Kong 999077, China

13 *Correspondence:* Tao He (taohers@whu.edu.cn), Zhaocong Wu (zcwoo@hnas.ac.cn)

14 **Highlights:**

- 15 • A novel method was developed to quantify Arctic surface SW CRE using long-term
16 GCF-CRK.
- 17 • GCF-CRK was directly estimated from observational data and incorporating spatiotemporal
18 information.
- 19 • Consideration of CF improved DSSR estimate accuracy by 8.7%~11.1% under partially
20 cloudy conditions.
- 21 • A stronger cloud-induced cooling effect over Greenland was revealed, with bias about 4
22 Wm⁻².
- 23 • A slower cloud cooling impact rate (1.131 Wm⁻² / decade) on Arctic surface SW radiation than
24 expected (1.64 Wm⁻² / decade).

25



26 **Abstract.** The surface shortwave cloud radiative effect (CRE) plays a critical role in modulating
27 the Earth's energy balance and climate change. However, accurately quantifying the CRE remains
28 challenging due to significant uncertainties in downwelling surface shortwave radiation (DSSR) and
29 cloud parameter estimates, especially in the Arctic. This paper introduces a novel approach that
30 enhances the accuracy of CRE estimation by constructing a computationally efficient, long-term
31 gridded surface cloud fraction radiative kernels (GCF-CRKs) and integrating refined DSSR estimates
32 and a high-precision cloud fraction (CF). By leveraging the correlation between the top-of-atmosphere
33 (TOA) shortwave radiative parameters and surface radiation, combined with high-precision fused CF
34 datasets from multiple satellite sources, we construct a CF-dependent model to refine DSSR estimates.
35 Based on this model, we construct GCF-CRKs using the CF as the sole perturbation parameter to
36 isolate the CF CRE. Our results indicate that this method significantly improves the accuracy of DSSR
37 estimation under partially cloudy conditions ($0 < CF < 100\%$), aligning more closely with ground-based
38 observations. In Arctic-wide validation experiments, the root mean square error (RMSE) was decreased
39 by approximately 2.5 Wm^{-2} , and the bias was reduced by 1.23 Wm^{-2} , which was an improvement of
40 8.7 % (reduction of RMSE) against the CERES-EBAF. The even greater improvements were achieved
41 at stations in Greenland (RMSE reduced by 4.53 Wm^{-2} and a bias reduced by $\sim 6.89 \text{ Wm}^{-2}$, with an
42 accuracy improved about 11.1%). The GCF-CRKs exhibit similar signs and patterns and enhanced
43 stability compared to existing kernels. The sensitivity analysis results reveal that seasonal and
44 interannual variations introduce GCF-CRK uncertainties of approximately $1 \text{ Wm}^{-2}\%$ and $0.1 \text{ Wm}^{-2}\%$,
45 respectively, while spatial variations within the same latitude range can cause CRK uncertainties of
46 $0.2\text{--}1.2 \text{ Wm}^{-2}\%$. These uncertainties can result in CRE biases ranging from 5 to 50 Wm^{-2} , which
47 demonstrates the limitations of existing methods that utilize short-term, small-area parameter data to
48 produce global CRKs. Using these GCF-CRKs, we estimated the spatiotemporal properties of the
49 surface shortwave CRE in the Arctic over a 21-year period (2000–2020), and the trend result indicates
50 that despite the increasing influence of the CF on the Arctic DSSR, the smaller magnitude and
51 interannual trend of the annual average surface shortwave CRE suggest that previous studies may have
52 overestimated the magnitude and rate of the cooling effect of clouds on the Arctic DSSR by up to 4
53 Wm^{-2} and 0.5 Wm^{-2} per decade, particularly in Greenland. This study provides a more accurate and
54 efficient assessment of the CRE, and the results underscore the need for more effective measures to
55 mitigate the impact of Arctic amplification on the surface radiative energy balance, which is crucial for
56 understanding and addressing regional and global climate change. The GCF-CRKs can be freely
57 available to the public at <https://doi.org/10.5281/zenodo.13907217> (Liu, 2024).

58 **Keywords:** Cloud fraction, Downwelling surface shortwave radiation, Cloud radiative kernel, Cloud
59 radiative effect



60 **1 Introduction**

61 The Arctic region is experiencing some of the most rapid and severe impacts of climate change, a
62 phenomenon often referred to as Arctic amplification (Baek et al., 2020). A key factor modulating this
63 amplification is the surface shortwave cloud radiative effect (CRE), which significantly influences the
64 energy balance and temperature distribution by regulating the surface energy fluxes, sea ice dynamics,
65 and overall climate feedback mechanisms in the Arctic (Yeo et al., 2022). Therefore, understanding and
66 accurately quantifying the CRE in the Arctic is crucial to improving climate models and predicting
67 future climate scenarios.

68 Despite its critical importance, accurate estimation of the CRE in the Arctic remains a significant
69 challenge due to the complex interplay between the atmospheric and surface conditions. Among the
70 various components that affect the CRE, downwelling Surface Shortwave Radiation (DSSR) is
71 particularly critical (Letu et al., 2020). The DSSR represents the solar radiation that reaches the Earth's
72 surface. Compared to radiative parameters at the top of the atmosphere (TOA), DSSR occurs beneath
73 the atmosphere and cannot be directly observed with precision by satellites. Instead, it must be
74 estimated indirectly using retrieval algorithms and auxiliary atmospheric data, resulting in increased
75 uncertainties (Pinker et al., 2005; Raschke et al., 2016). Much of these uncertainties stem from
76 inaccurate estimations of the complex perturbing factors.

77 Clouds, which are widely present in the atmosphere, strongly regulate both the direction and
78 magnitude of DSSR, making them a crucial parameter for global and regional energy budgets (Matus
79 and L'ecuyer, 2017). Since the release of the Fifth Assessment Report of the Intergovernmental Panel
80 on Climate Change (IPCC) (AR5), the accuracy of DSSR flux datasets has improved continuously, but
81 the uncertainty introduced by cloud parameters remains one of the most significant challenges in
82 climate model predictions (Ipcc, 2022). The optical depth (TAU), altitude, thickness, and phase of
83 clouds all have complex effects on the scattering and absorption of shortwave radiation, and the
84 uncertainties of these factors directly impact the accuracy of radiative forcing estimates and climate
85 change predictions (Boucher O et al., 2013). Among these factors, the cloud fraction (CF), i.e., the
86 horizontal area of the Earth's surface covered by clouds, has been identified as a key indicator affecting
87 the accuracy of DSSR estimates, thereby modulating the CRE (Hahn et al., 2001; Liu et al., 2011).
88 Compared to cloud-free conditions, clouds reduce the incoming solar radiation by 49 Wm^{-2} ,
89 approximately 14% of the total incident solar radiation, and deviations in the CF can lead to DSSR
90 differences ranging from 10 to 90 Wm^{-2} (Wild et al., 2019). In high-latitude regions, such as the Arctic,
91 differences in the DSSR caused by significant CF deviations are even more pronounced (Liu et al.,
92 2022). Using reanalysis data, Kay et al. found that the decrease in the CF has led to a significant
93 increase in the DSSR in the Arctic (Kay and L'ecuyer, 2013). Sledd and L'Ecuyer studied the



94 interannual variability of the CF's impact on Arctic surface shortwave absorption trends and found that
95 substantial differences in the CF between datasets can introduce uncertainty in the lag effects of the
96 response of the DSSR trend (Sledd and L'ecuyer, 2019; Sledd and L'ecuyer, 2021).

97 Some studies have focused on quantifying the impacts of cloud parameters on the Arctic DSSR.
98 By analyzing the correlation between the CF changes and the DSSR across five reanalysis datasets, Zib
99 et al. found that CF deviations could result in monthly surface shortwave (SW) flux discrepancies of
100 greater than 90 Wm^{-2} in some reanalysis datasets (Zib et al., 2012). By comparing the relationship
101 between the CF and SW in four reanalysis datasets, Walsh et al. discovered that deviations in the
102 coverage of low-level clouds during the Arctic summer could cause seasonal discrepancies of
103 approximately 160 Wm^{-2} (Walsh et al., 2009). Other studies have used similar correlation methods to
104 analyze parameters from satellite observations, model simulations, and reanalysis data and have
105 concluded that CF deviations in the Arctic could lead to annual average DSSR discrepancies of greater
106 than $10\text{--}40 \text{ Wm}^{-2}$ (Hakuba et al., 2017; Huang et al., 2017; Kato et al., 2018). These values greatly
107 exceed the impact of cloud parameter differences on the annual global DSSR (Kato et al., 2011).

108 However, the challenges in accurately estimating the DSSR directly impact the accuracy of the
109 CRE estimation, complicating the understanding of Arctic radiative processes. Currently, DSSR
110 estimation methods often rely on mixed model algorithms that primarily address two extreme
111 conditions: overcast skies (CF=100%) and clear skies (CF=0%). For partially cloudy conditions
112 ($0 < \text{CF} < 100\%$), these methods typically combine clear-sky parameterization schemes with existing
113 cloud products and use empirical formulas to derive indirect estimates (Chen et al., 2020). They do not
114 delve deeply into the radiative transfer mechanisms between cloud properties and DSSR, leading to
115 error accumulation and significant biases in DSSR estimates. Consequently, these biases directly
116 impact the accuracy of CRE estimation, further complicating the understanding of Arctic radiative
117 processes.

118 In addition to the inherent accuracy of the parameters, how to extract the corresponding radiative
119 contributions from complex perturbation factors is also crucial for enhancing the precision of CRE
120 estimation. Currently, there are three main methods for isolating the radiative contributions of
121 individual influencing factors. The first is the data simulation method, such as using radiative transfer
122 models to simulate the transmission of radiative parameters in the atmosphere and on the surface and
123 quantifying the radiative effect due to cloud properties by inputting additional atmospheric information
124 (Kato et al., 2012; Kim and Ramanathan, 2008). Alternatively, cloud properties simulated using
125 satellite simulators can be converted into synthetic observations obtained from satellite observation
126 systems to isolate the impact of cloud deviations on surface radiative parameters in models. However,
127 low-accuracy CF information introduces significant estimation errors. The second commonly used



128 method is the partial perturbation algorithm, initially proposed by Wetherald and Manabe (Wetherald
129 and Manabe, 1988). This method separates TOA radiative flux changes caused by specific variables by
130 taking the difference between global climate model variation experiments and perturbation experiments.
131 While this method can directly calculate various climate feedbacks, it requires rerunning the global
132 climate model for each slight parameter change, demanding high computational resources and resulting
133 in a low operational efficiency (Loeb et al., 2018b).

134 The current radiative kernel method, widely used in evaluating climate feedback, constructs a
135 radiative kernel by constraining the change in a single variable due to a small perturbation. This kernel
136 is used as a constant factor to calculate the perturbation effects of the variable on the radiative flux over
137 different time periods and regions (Soden et al., 2008; Zhou et al., 2022). This method requires
138 significantly less overall computation than the partial perturbation algorithm and can effectively reduce
139 correlation errors between different influencing factors. However, due to the vertical nonlinearity effect
140 of cloud parameters, directly estimating the cloud radiative kernel is challenging. Therefore, non-cloud
141 radiative kernels, such as those for temperature, water vapor, and surface albedo, are often used to
142 indirectly estimate the CRE (Vial et al., 2013). This approach can confuse radiative uncertainties caused
143 by non-cloud parameters with the CRE, thereby increasing the estimated radiative contribution of
144 clouds.

145 To directly isolate the radiative contribution of the CF, Thorsen et al. applied a partial radiative
146 perturbation-like calculation to observational datasets and proposed an observation-based partial
147 perturbation method, namely, the clouds and the Earth's Radiant energy system-partial radiative
148 perturbation (CERES-PRP) (Thorsen et al., 2018). This method calculates radiative kernels by flexibly
149 combining perturbation variables to achieve flux perturbation calculations. It has been successfully
150 applied to CERES-energy balanced and filled (EBAF) surface radiative parameters (Kato et al., 2018)
151 and long-term studies of Earth's energy budget changes (Loeb et al., 2018a). However, this method
152 calculates kernels using control operations from a single year and neglects the spatiotemporal
153 variability of the parameters, which can lead to significant temporal and regional errors (Kramer et al.,
154 2019). Additionally, similar to most current radiative kernels, this method focuses on TOA radiative
155 budgets and pays insufficient attention to surface radiative budgets and the associated radiative forcing
156 contributions.

157 To achieve a higher CRE estimation accuracy, in this study, we used improved DSSR and
158 higher-precision CF data to construct long-term, gridded surface cloud fraction radiative kernels
159 (GCF-CRKs) and incorporated the spatiotemporal variability. These new CRKs were then used to
160 accurately quantify the contribution of the CF to the DSSR and to enable detailed estimation and
161 analysis of the spatiotemporal characteristics and long-term trends of the surface shortwave CRE in the



162 Arctic. Section 2 of this paper introduces the observational data. Section 3 provides the details of the
163 method for constructing CRKs, In Section 4, the corrected DSSR and the CRE are estimated using the
164 CF-CRKs, and the accuracies are validated. Section 5 presents the discussion and conclusions.

165 **2 Data**

166 **2.1 Satellite Observational Datasets: CERES-SYN1deg and CERES-EBAF**

167 The CERES-syntopic 1° (SYN1deg) dataset is recognized as one of the most accurate global
168 radiative energy balance products, particularly for mid-latitude regions. However, its accuracy in
169 high-latitude areas remains highly uncertain(Jia et al., 2016; Jia et al., 2018). Studies have shown that
170 in high-latitude regions, the RMSE of the CERES-SYN1deg exceeds 33.56 Wm⁻², and the bias is
171 greater than 3.43 Wm⁻². This reduced accuracy is likely caused by the significant errors in regions
172 covered by ice and snow(Inamdar and Guillevic, 2015). Moreover, several studies have demonstrated
173 that using more accurate cloud parameters can significantly improve its accuracy, indicating that the
174 inaccuracies in the cloud parameters contribute to the observed errors(Kato et al., 2011; Thorsen et al.,
175 2018).

176 The CERES-EBAF (datasets, including the CERES-EBAF-TOA and CERES-EBAF-surface
177 radiative fluxes, are also highly accurate global monthly gridded (1°×1°) datasets. In the EBAF
178 products, CERES shortwave and longwave radiative fluxes are adjusted within their measurement
179 uncertainties to ensure that the CERES's long-term global annual average net flux is consistent with
180 long-term ocean heat storage data(Loeb et al., 2019). The EBAF-surface flux calculation utilizes the
181 National Aeronautics Space Administrations' (NASA) Langley-adjusted Fu–Liou radiative transfer
182 model, which incorporates cloud properties retrieved from CERES-moderate resolution imaging
183 spectroradiometer (MODIS), meteorological data from reanalysis systems, and aerosol data from the
184 aerosol assimilation system, and the calculation of the surface irradiance is constrained by the
185 CERES-observed TOA irradiance. Christensen et al. compared various radiative parameter products for
186 the Arctic and found that the CERES-EBAF represents the average level of these products, suggesting
187 that this dataset should be considered a key benchmark for evaluating Arctic surface radiative
188 budgets(Christensen et al., 2016).

189 **2.2 Ground-based Observation Datasets**

190 Over the past few decades, globally distributed ground-based radiative flux networks have
191 provided extensive observation validation datasets for satellite observations. Compared to other global
192 regions, the Arctic has a sparse distribution of surface radiative flux stations, and most located in



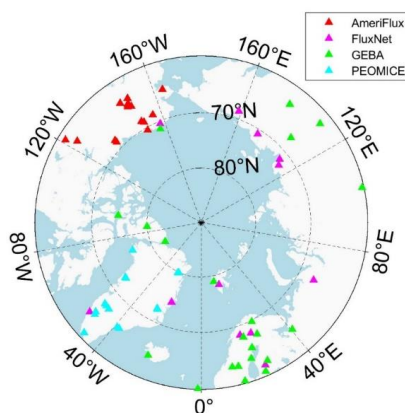
193 terrestrial areas. Nevertheless, these ground stations offer reliable reference data for Arctic radiative
194 fluxes.

195 (1) AmeriFlux

196 AmeriFlux is part of the U.S. flux station network, which is jointly managed by the U.S.
197 Department of Energy's National Energy Technology Laboratory (NETL) and the U.S. Department of
198 Agriculture (USDA). It is an atmospheric flux observation network that primarily monitors and
199 quantifies carbon, water, and energy fluxes in terrestrial ecosystems. This network spans various
200 geographical locations and ecosystems in the U.S., including forests, grassland, wetlands, and cropland.
201 AmeriFlux station data have been widely used to evaluate surface radiative fluxes (Chen et al., 2020).
202 In this study, we used data from 18 stations located above 60°N, primarily in northern and western
203 Alaska, covering diverse ecosystem types such as tundra, wetlands, and forests.

204 (2) FluxNet

205 FluxNet is one of the world's largest networks for monitoring and quantifying carbon, water, and
206 energy fluxes in terrestrial ecosystems. FluxNet includes several stations located above 60°N, and some
207 overlap with AmeriFlux. In this study, DSSR data from 13 stations were selected.



208

209 **Figure 1. Spatial distribution of 66 ground stations in four radiation flux networks**

210 (3) GEBA

211 The Global Energy Balance Archive (GEBA) is a centralized database that contains measurements
212 of surface energy fluxes worldwide. The GEBA compiles monthly average data for various radiative
213 energy balance fluxes observed at the Earth's surface, including global radiation (total DSSR), diffuse
214 and direct shortwave radiation, surface albedo, reflected shortwave radiation, downwelling and
215 upwelling longwave radiation, net radiation, sensible and latent heat fluxes, ground heat flux, and latent
216 heat of melting. In the Arctic region, the GEBA includes numerous stations, including both ocean



217 buoys and land-based observation stations, providing ground-truth data for surface radiation
218 observations in this region(Wild et al., 2017). In this study, data from22 stations collected during
219 2000–2020 were selected.

220 (4) PROMICE

221 The Programme for Monitoring of the Greenland Ice Sheet (PROMICE) is a project designed to
222 monitor changes in the Greenland Ice Sheet (GrIS). This network covers the western, central, and
223 eastern parts of Greenland, and variables such as surface height changes, snow depth, temperature,
224 humidity, and the impact of global climate change on the ice sheet are monitored (Ahlstrom and Team,
225 2011). The PROMICE stations are in a variety of ecosystems, including alpine, glacier, and coastal
226 areas and use automated instruments and sensors to measure atmospheric and surface variables at a
227 high frequency (typically hourly), such as the temperature, humidity, air pressure, wind speed, snow
228 depth, and surface height. In this study, data from 14 stations collected during 2000–2020 were
229 selected as the validation data.

230 (5) Data Processing and Quality Control

231 FluxNet and GEBA directly provide monthly mean flux data, while AmeriFlux provides
232 observations every 30 minutes, and PROMICE provides hourly data. To better validate the monthly
233 mean satellite data, a consistent resampling process is required. The 30-minute and hourly data are first
234 averaged to daily values, and then monthly averages are obtained, minimizing the impact of missing
235 values (Roesch et al., 2011). Before aggregating the data into monthly averages, rigorous quality
236 control must be performed(Jiang et al., 2015). In this study, the data quality was first assessed, and the
237 original data with poor quality marks were removed. The data continuity was then checked, and the
238 monthly shortwave radiation values were calculated only when the daily valid data exceeded 3 hours
239 and the monthly valid data exceeded 15 days.

240 **2.3 Fusion CF Dataset**

241 High-precision CF information is crucial for obtaining accurate GCF-CRKs. However, existing
242 CF datasets are mostly based on single-satellite data, leading to a low accuracy, discontinuous
243 spatiotemporal coverage, and significant spatiotemporal differences between datasets. To address this,
244 we developed a spatiotemporal fusion framework for multiple-satellite CF products, leveraging their
245 complementary strengths of spatiotemporal completeness and accuracy. We produced a high-precision,
246 spatiotemporally complete, $1^{\circ}\times 1^{\circ}$ monthly average CF dataset for the Arctic region from 2000 to
247 2020(Liu et al., 2023). This method enhances the accuracy of passive sensor data using a cumulative
248 distribution function matching algorithm with spatiotemporal extension, and then, it employs a
249 Bayesian maximum entropy fusion algorithm to integrate multiple observation datasets with



250 uncertainties. The final fused dataset yields a 10–20% overall reduction in the inconsistencies between
251 active sensor data and ground observations, and yields more significant improvements in
252 snow/ice-covered regions. The fused product has a better consistency with reanalysis and model data
253 and maintains high spatiotemporal completeness within the study period and region. The specific data
254 can be downloaded from <https://doi.org/10.5281/zenodo>.

255 3 Principles and Methods

256 3.1 Single-layer Cloud Radiative Transfer Model

257 In remote sensing observations, satellites can directly measure the TOA radiative flux, but the
258 DSSR must be retrieved through inversion. Traditionally, to obtain surface radiative parameters, TOA
259 parameters are used to constrain the surface parameter inversion (Kato et al., 2018; Loeb et al., 2018b).

260 For the shortwave radiative flux, the TOA albedo α_A and atmospheric absorption a are defined as
261 follows:

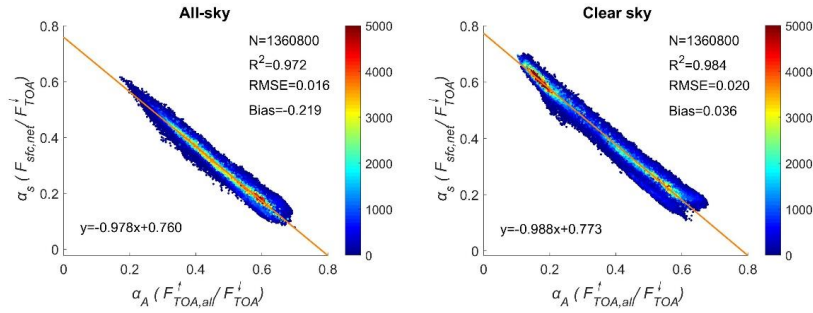
$$262 \quad \alpha_A = \frac{F_{TOA,all}^\downarrow}{F_{TOA}^\downarrow}, \quad (1)$$

$$263 \quad a = \frac{(F_{TOA}^\downarrow - F_{TOA,all}^\downarrow) - (F_{sfc,all}^\downarrow - F_{sfc,all}^\uparrow)}{F_{TOA}^\downarrow}. \quad (2)$$

264 Based on the principle of energy conservation,

$$265 \quad \alpha_A + a = 1 - \frac{F_{sfc,all}^\downarrow - F_{sfc,all}^\uparrow}{F_{TOA}^\downarrow} = 1 - a_s, \quad (3)$$

266 where α_A is the ratio of the reflected energy at the TOA to the total incident energy, and a_s is the
267 surface absorption rate, i.e., the ratio of the energy absorbed at the surface to the total incident energy
268 at the TOA. In this context, α_A can be expressed as a function of a_s , linking the TOA shortwave flux to
269 the surface shortwave flux. Assuming that the surface albedo does not significantly vary with the
270 seasons within a $1^\circ \times 1^\circ$ grid, a strong linear relationship exists between α_A and a_s . The slope of this
271 linear relationship depends on the variation in the atmospheric absorption a relative to the surface
272 absorption a_s .



273

274 **Figure 2. Relationship between the albedo at the top of the atmosphere and the absorption ratio at the**
 275 **surface**

276 Analysis of CERES-SYN1deg $1^\circ \times 1^\circ$ monthly average data for the Arctic region revealed that
 277 there is a strong linear correlation between α_A and α_s , with a correlation coefficient (R^2) of 0.97 and a
 278 root mean square error (RMSE) of 0.016. This linear relationship indicates that TOA SW parameters
 279 can effectively constrain DSSR estimation. If the TOA SW and surface radiative parameters and cloud
 280 properties are known, the DSSR can be estimated for a given region. For clear-sky conditions, R^2
 281 improves to 0.984 and the bias is 0.04; whereas for cloudy conditions, R^2 slightly decreases and the
 282 bias increases to 0.22. This discrepancy is primarily due to the greater uncertainty introduced by cloud
 283 parameter errors in estimating the surface radiative parameters (Liu et al., 2022). Therefore, we propose
 284 a method to estimate the DSSR using TOA observations and clear-sky radiative flux while
 285 incorporating CF information into the radiative transfer calculations to isolate the sensitivity of the
 286 DSSR to the CF among various cloud parameters.

287 Assuming the surface is a Lambertian reflector, the DSSR can be calculated as follows:

$$288 \quad F_{sfc,all}^\downarrow = F_0(\mu_i) + F_m(\mu_i), \quad (4)$$

289 where $F_0(\mu_i)$ is the DSSR in the absence of the surface contribution, and the second term accounts for
 290 the multiple reflection effects between the atmosphere and the bright surface. μ_i is the cosine of the
 291 solar zenith angle. When considering the impact of CF, $F_0(\mu_i)$ is weighted by f :

$$292 \quad F_0(\mu_i) = fF_{sfc,cld}^\downarrow + (1-f)F_{sfc,ctr}^\downarrow, \quad (5)$$

293 where $F_{sfc,cld}^\downarrow$ is the surface downward radiative flux under cloudy conditions and zero surface albedo,
 294 and $F_{sfc,ctr}^\downarrow$ is the surface downward radiative flux under clear-sky conditions. According to Liu et al.
 295 and Xie et al., $F_{sfc,cld}^\downarrow$ can be expressed as a function of $F_{sfc,ctr}^\downarrow$ (Liu et al., 2011; Xie et al., 2014):

$$296 \quad F_{sfc,cld}^\downarrow = (1-\alpha)F_{sfc,ctr}^\downarrow, \quad (6)$$

$$297 \quad \alpha = \alpha_{cld,0} + \alpha_{cld,0}, \quad (7)$$



298 where $\alpha_{cld,0}$ is the cloud albedo, and $a_{cld,0}$ is the cloud absorption rate. The subscript 0 indicates the
 299 case with zero surface albedo. Typically, the cloud absorption rate is much smaller than the cloud
 300 albedo (Gautier and Landsfeld, 1997; Xie et al., 2014), and thus, it can be neglected for simplification.
 301 Consequently, $F_0(\mu_i)$ can be expressed as

$$302 \quad F_0(\mu_i) = (1 - \alpha_{cld,0}f)F_{sfc,ctr}^\downarrow. \quad (8)$$

303 To the first order, the cloud albedo is the primary factor that maintains the close relationship
 304 between the CF and planetary albedo (or the reflected SW at the TOA), which has been demonstrated
 305 in various observation records (Norris and Evan, 2015). To further calculate the cloud albedo, we
 306 introduce the concept of the effective cloud albedo (Betts and Viterbo, 2005; Liu et al., 2010).

$$307 \quad \alpha_{SRF,cld} = -\frac{F_{sfc,all}^\downarrow - F_{sfc,ctr}^\downarrow}{F_{sfc,ctr}^\downarrow} = 1 - \frac{F_{sfc,all}^\downarrow}{F_{sfc,ctr}^\downarrow}. \quad (9)$$

308 The effective cloud albedo $\alpha_{SRF,cld}$ is mathematically similar to the surface albedo but is a
 309 dimensionless value. Liu et al. have shown that when accounting for multiple reflection effects
 310 between clouds and the surface, $\alpha_{SRF,cld}$ can be approximated as the product of the cloud albedo,
 311 surface albedo, and CF (Liu et al., 2011). Thus,

$$312 \quad \text{Equation.} \quad (10)$$

$$313 \quad \text{For conditions with } r_s=0, \alpha_{SRF,cld,0} = 1 - \frac{F_0}{F_{sfc,ctr}^\downarrow} = \alpha_{cld,0}f. \quad (11)$$

314 To compute the effective cloud albedo, both the numerator and denominator of Equation (9) are
 315 multiplied by a function of the surface albedo:

$$316 \quad \alpha_{SRF,cld} = 1 - \frac{F_{sfc,all}^\downarrow - F_{sfc,all}^\uparrow}{F_{sfc,ctr}^\downarrow(1-r_s)}. \quad (12)$$

317 Thus,

$$318 \quad (1 - r_s)(1 - \alpha_{SRF,cld})F_{sfc,ctr}^\downarrow = F_{sfc,all}^\downarrow - F_{sfc,all}^\uparrow, \quad (13)$$

319 which represents the net SW at the surface. Based on previous analyses, the surface absorption rate a_s
 320 can similarly be expressed as a function of the surface net SW. Therefore, the effective cloud albedo
 321 can be expressed as a function of the incident shortwave radiation at the TOA and the surface
 322 absorption rate:

$$323 \quad F_{TOA}^\downarrow a_s = (1 - r_s)(1 - \alpha_{SRF,cld})F_{sfc,ctr}^\downarrow. \quad (14)$$

324 Considering that a_s can be modeled as a linear function of the TOA albedo, the corresponding
 325 cloud albedo can be computed using TOA observations, the clear-sky surface SW, and the CF.



326 For a Lambertian surface, the influence of the cloud parameters on diffuse radiation is more
 327 pronounced under cloudy conditions. When considering multiple reflection effects, the net SW at a
 328 surface with a surface albedo r_s is

$$329 \quad F_m = F_0 \frac{r_s \alpha_{A,cl,d} f T^2}{1 - r_s \alpha_{A,cl,d} f T^2}, \quad (15)$$

330 where T is the transmissivity of the atmosphere to diffuse radiation under cloudy conditions, which is
 331 dependent on various atmospheric factors such as aerosols, ozone, and water vapor (Huang et al., 2018).
 332 For simplification, in this study, we used empirical parameters combined with observational data.

$$333 \quad T = \frac{T_{all} - (1-f)r_{clr}}{f} = \frac{F_{diff,all}^{1-f} F_{diff,clr}^f}{f F_{TOA}^1}. \quad (16)$$

334 Ultimately, the all-sky DSSR can be expressed as a function of the satellite-observed TOA
 335 shortwave radiation, clear-sky DSSR, and CF. In this study, we focused only on the CRE related to CF
 336 perturbations. Therefore, based on the partial perturbation approach, CF is the sole user-defined
 337 variable in Equation (14), and the other unknown parameters are consistent with the original
 338 CERES-SYN1deg data.

339 3.2 Separation Method for CF Radiation Contribution Based on Observational Data

340 To isolate the sensitivity of radiative flux changes to the CF from observational data, we
 341 developed GCF-CRKs. In traditional CRK algorithms, it is assumed that the perturbation in the flux is
 342 linearly related to the perturbation itself, and thus, it is necessary to calculate the CRKs for each
 343 atmospheric layer individually, which are then summed. In this study, based on the plane-parallel
 344 approximation principle, we utilized the full-layer CF. Within the finite difference framework and in
 345 conjunction with the CERES-SYN1deg observational data, it is possible to compute the full-layer
 346 CF-CRKs.

347 According to Thorsen et al., the essence of partial radiative perturbation methods lies in different
 348 forms of finite difference approximations. In this study, the factor influencing the radiative parameters
 349 is the CF (f). When it changes by Δf , according to the finite difference principle, the effect on the
 350 radiative flux δF is

$$351 \quad \delta F_{\Delta f,c}^p = F(\bar{f} + \Delta f, \bar{c}_1, \dots, \bar{c}_n) - F(\bar{f}, \bar{c}_1, \dots, \bar{c}_n) + \phi_c^p(\Delta f), \quad (17)$$

352 where F is the all-sky DSSR, and Δf is the perturbation of the variable relative to its initial climate
 353 mean \bar{f} , i.e., $\Delta f = f - \bar{f}$. The climate mean value refers to the average of all of the data for a specific
 354 calendar month (April–September in this study) within the time series. All of the other variables related
 355 to the radiative transfer are represented as $\bar{c}_1, \dots, \bar{c}_n$. $\phi_c^p(\Delta f)$ is the truncation error of the forward



356 finite difference. The subscript C indicates that the flux perturbation is related to the climate monthly
357 mean initial state. To minimize the impacts of temporal and spatial variabilities of the CF on the results,
358 we prefer to calculate the flux perturbations related to the monthly mean values:

$$359 \quad \delta F_{\Delta f, M}^p = F(f + \Delta f, c_1, \dots, c_n) - F(f, c_1, \dots, c_n) + \phi_M^p(\Delta f) \quad (18)$$

360 where f is the monthly mean CF, and the subscript M indicates that the flux perturbation is related to
361 the monthly mean baseline state. In this equation, the truncation error is of the same order of magnitude
362 as the perturbation variable itself, meaning that the computed perturbation flux is influenced not only
363 by the perturbation variable but also by the potential decorrelation between the perturbation and
364 non-perturbation variables. To minimize this, a central finite difference approach can be used to
365 improve the magnitude of the order of the accuracy. Thus, backward finite differences are introduced.

$$366 \quad \delta F_{\Delta f, M}^b = F(f, c_1, \dots, c_n) - F(f - \Delta f, c_1, \dots, c_n) + \phi_M^b(\Delta f). \quad (19)$$

367 Averaging the perturbation values obtained from the two finite difference calculations yields

$$368 \quad \delta F_{\Delta f, M} = \frac{[F(f + \Delta f, c_1, \dots, c_n) - F(f, c_1, \dots, c_n)] + [F(f, c_1, \dots, c_n) - F(f - \Delta f, c_1, \dots, c_n)]}{2} + \phi_M(\Delta f^2). \quad (20)$$

369 While central differences can reduce the impact of the decorrelation between the related variables,
370 the perturbation states $f + \Delta f$ and $f - \Delta f$ may exceed the physical limits of the parameters, making them
371 impractical for radiative transfer calculations. Therefore, a two-step alternative is proposed: when the
372 CF perturbation state is invalid, initially, the monthly climate mean value is used in place of the
373 corresponding monthly average. If the substituted value is still non-physical, it is replaced with the
374 nearest valid CF value within the effective range. Finally, the central difference is applied to compute
375 the radiative perturbation.

376 To further simplify the quantification process of the = CRE due to CF perturbations, in this study,
377 we used Thorsen et al.'s method in the CERES-model by replacing the fixed perturbations with the
378 observed variable anomalies. This means normalizing the perturbation effects of the variable on the
379 radiative perturbation to calculate the CRKs. In this concept, the resulting CF-CRKs are a byproduct of
380 the central difference calculations, representing the contribution of a 1% CF change to the DSSR.

$$381 \quad K_{\Delta f} = \frac{\delta F_{\Delta f}}{\Delta f}. \quad (21)$$

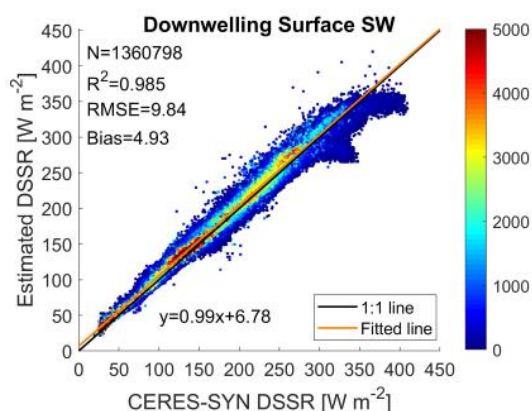
382 Using the high-precision fused CF dataset and CERES observational data, GCF-CRKs can be
383 obtained. The computed full-layer CRK, in combination with the fused CF dataset, allows for
384 correction of the biases in the CERES DSSR data.



385 **4 Results and Validation**

386 **4.1 DSSR Estimated Using the Single-layer Cloud Radiative Transfer Model**

387 In this study, we used the single-layer cloud radiative transfer model constructed in Section 3.1 to
388 estimate the DSSR received at the surface under partly cloudy conditions. To verify the accuracy and
389 applicability of this model, we compared the estimated results with the DSSR provided by the
390 CERES-SYN dataset.



391

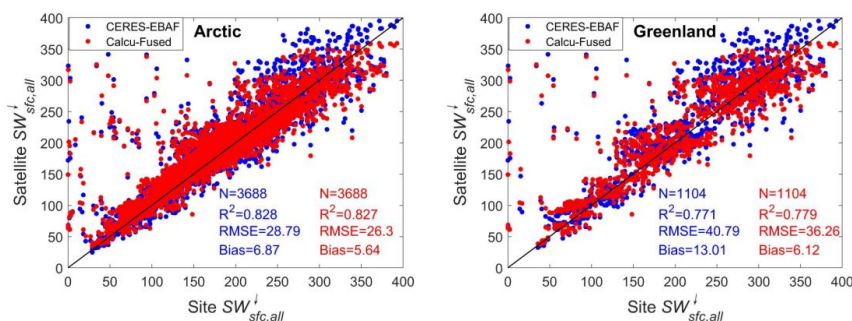
392 **Figure 3. Scatter plot comparing the DSSR estimated using the single-layer cloud radiative transfer**
393 **model with the CERES-SYN DSSR dataset.**

394 Figure 3 displays a scatter plot comparing the grid-point DSSR estimates with CERES-SYN data
395 for the Arctic region. It is evident from the plot that the estimates obtained using our single-layer cloud
396 radiative transfer model have a high degree of consistency with the CERES-SYN DSSR data.
397 Specifically, the R^2 value between the estimates and observations is 0.985, indicating a very strong
398 positive correlation. Moreover, the RMSE is approximately 9.69 W m^{-2} , which is considered to be a
399 small error in the field of radiative estimation, further confirming the model's accuracy. Additionally,
400 the bias is approximately 5 W m^{-2} , indicating that the average deviation between the estimated and
401 CERES-SYN DSSR values is relatively small, which suggests that the model generally provides
402 accurate DSSR estimates. This result demonstrates that using TOA observations, clear-sky surface
403 shortwave radiation, and CF information to estimate the DSSR under all-sky conditions is highly
404 feasible.

405 Using more accurate CF information, we corrected the bias in the CERES DSSR data. Ground
406 station observations are often considered to be effective data for validating the accuracy of satellite
407 radiative parameter retrievals (Chen et al., 2020). We compared the estimated DSSR with the
408 CERES-EBAF DSSR and conducted a quantitative evaluation using monthly mean DSSR observations



409 from 66 Arctic ground stations. The R^2 , RMSE and bias were used as evaluation metrics. Figure 4
410 shows scatter plots comparing the estimated DSSR with the CERES-EBAF DSSR and ground
411 observations. In Figure 4, each point represents a monthly mean DSSR in a $1^\circ \times 1^\circ$ grid bin. The plot
412 shows that our estimated DSSR is more consistent with the ground observations compared to the
413 CERES-EBAF data. Specifically, for the entire Arctic region, the data of the scatter plot of the
414 estimated DSSR versus ground observations (red) have an R^2 value similar to that of the CERES-EBAF
415 versus ground observations (blue). However, the RMSE of the estimated DSSR is 26.3 W m^{-2} , which is
416 approximately 2.5 W m^{-2} lower than the value of 28.79 W m^{-2} for the CERES-EBAF data, which is an
417 improvement of 8.7 %. The bias between the estimated DSSR and ground observations is also reduced
418 by 1.23 W m^{-2} compared to that of the CERES-EBAF data. This indicates that when using ground
419 observations as a reference, our estimated DSSR generally has smaller deviations and a better stability.
420 When focusing on GrIS, the R^2 value of our estimated DSSR is slightly higher than that of the
421 CERES-EBAF data, i.e., by 0.008, but the reductions in the RMSE and bias are more significant, i.e.,
422 4.53 W m^{-2} and 6.89 W m^{-2} , respectively. This means the estimate accuracy improved about 11.1 %.
423 English et al. and Huang et al. found that the CERES-EBAF DSSR dataset overestimates the DSSR by
424 approximately 8.86 to 13 W m^{-2} in the Arctic (English et al., 2015; Christensen et al., 2016). The
425 corrected DSSR values obtained in this study significantly improve this overestimation, with more
426 notable improvements in the GrIS.

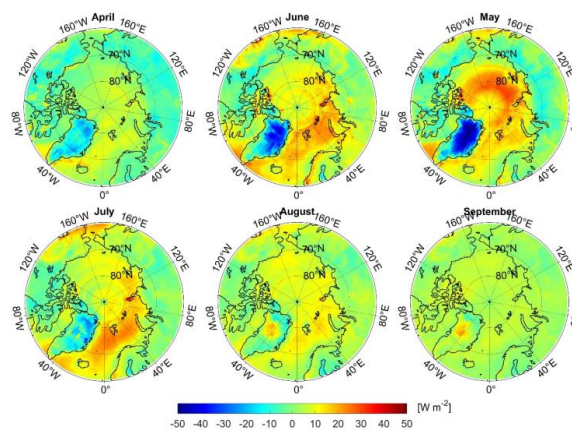


427
428 **Figure 4. Scatter plot comparing the estimated DSSR, CERES-EBAF DSSR, and ground observations**

429 To further analyze the differences between the estimated DSSR and CERES-EBAF DSSR, we
430 conducted spatiotemporal difference analysis of the two datasets (Figure 5). Temporally, we observed
431 that the estimated DSSR and CERES-EBAF DSSR exhibit a high degree of consistency in terms of
432 their trends and magnitudes. Specifically, the maximum area-weighted average DSSR in the Arctic
433 region occurred in June, with a value of approximately 250 W m^{-2} , while the minimum occurred in
434 September, with a value of approximately 78 W m^{-2} . Further analysis revealed that during the spring
435 (April–June), our estimated DSSR values are generally lower than the CERES-EBAF observations, and
436 the largest underestimation occurred in April, i.e., approximately 13 W m^{-2} . However, from late



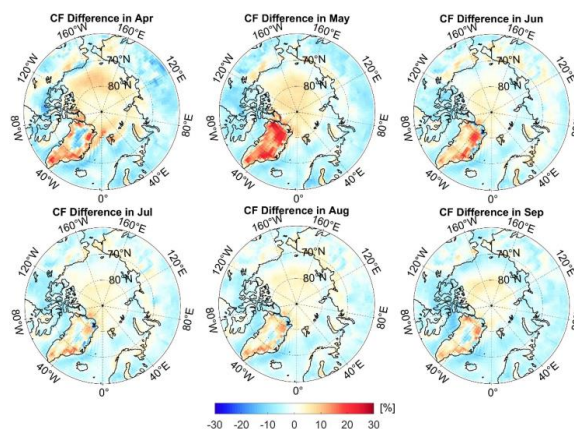
437 summer to autumn (July–September), the estimated DSSR was slightly higher than the EBAF DSSR,
438 and the maximum overestimation occurred in August, with a value of approximately 5 W m^{-2} . Spatially,
439 the bias between the estimated DSSR and the CERES-EBAF DSSR exhibits significant variation
440 across the different geographic locations. In land areas, particularly along the land-sea boundaries and
441 certain regions of Greenland, our estimated DSSR exhibits notable underestimation, with biases
442 exceeding 10 W m^{-2} from April to July. Conversely, in the oceanic regions, especially the open sea, our
443 estimated DSSR is slightly higher than the CERES-EBAF DSSR.



444

445 **Figure 5. Spatiotemporal distribution of the difference between the estimated DSSR and CERES-EBAF**
446 **DSSR.**

447 We performed bias attribution analysis using CF data and calculated the spatiotemporal
448 differences between the fused CF dataset and CERES- single scanner footprint (SSF) CF data (Figure
449 6). From the CF difference map, we observed that there is a high degree of consistency between the
450 regions of underestimation of our estimated DSSR and the areas where the SSF CF is lower than the
451 fused CF, particularly along land edges and in the GrIS. This suggests that the CERES series data
452 underestimates the CF in these areas, leading to overestimation of the DSSR. However, in the ocean
453 areas that where are not perennially covered by sea ice (perennially open waters), the SSF CF
454 significantly higher than the fused CF (indicated by negative values of the fused CF minus the SSF CF
455 in Figure 6), suggesting that the CERES DSSR values in these regions are likely underestimated. In
456 contrast, in the central Arctic Ocean, the fused CF is notably higher than the SSF CF. Given the
457 negative correlation between the CF and DSSR, the estimated DSSR should be lower in this area,
458 which is contrary to our previous findings. Therefore, when using the estimated DSSR, careful
459 consideration should be given to the results for the central Arctic Ocean.

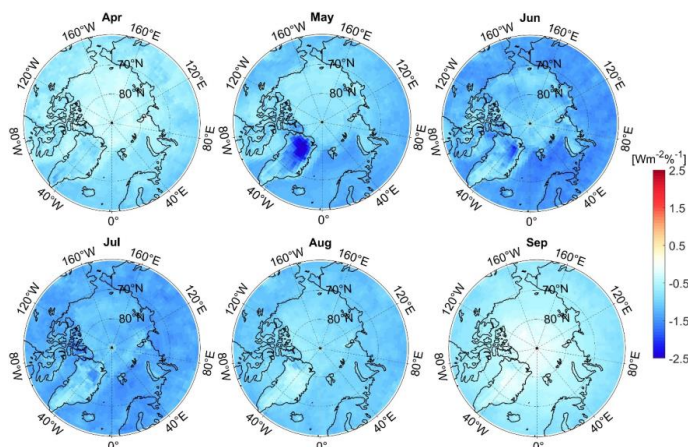


460

461 **Figure 6. Spatiotemporal distribution of the difference between the fused CF and CERES-SSF CF.**

462 **4.2 Temporal and Spatial Characteristics of GCF-CRKs**

463 Figure 7 presents the monthly mean GCF-CRK for the surface SW in different months. A positive
464 value, shown in red, corresponds to radiative heating within the system; while a negative value, shown
465 in blue, represents radiative cooling. Notably, all of the grids of the GCF-CRKs in the Arctic are
466 uniformly negative from April to September, but their magnitudes vary spatially and temporally.
467 Temporally, the surface GCF-CRKs exhibit smaller negative values in April, August, and September,
468 with monthly averages of less than $-1 \text{ Wm}^{-2}\%$. Conversely, in May, June, and July, the overall mean
469 values exceed $-1.5 \text{ Wm}^{-2}\%$, indicating that during these summer months, a 1% change in the CF
470 contributes more significantly to the cooling effect on the surface shortwave radiation. Spatially, the
471 GCF-CRKs' values over the oceanic regions are generally lower than those over the land, suggesting
472 that changes in the CF have a greater radiative impact over the land. The most substantial negative
473 values are located over Greenland, particularly in the northern region during May where the kernel
474 exceeds $-2.5 \text{ Wm}^{-2}\%$. This is associated with intense cyclonic activity in the area.



475

476

Figure 7 Monthly mean GCF-CRKs from April to September

477

478

479

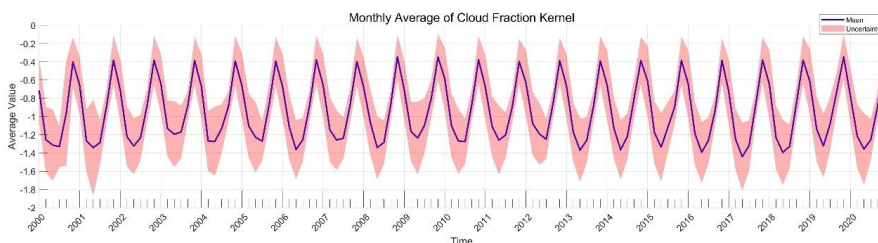
480

481

482

483

Over the time series, the GCF-CRK displays a clear temporal pattern, with its absolute value increasing from April to June, peaking in June at $-1.3 \text{ Wm}^{-2}\%^{-1}$, followed by a decline toward September. However, the uncertainty is also highest during this season, mainly due to the increased solar radiation at lower latitudes of the Arctic during summer, while higher latitudes still receive relatively low incoming radiation. Additionally, parameters such as CF, TAU, and cloud top pressure (CTP) exhibit significant spatial heterogeneity, leading to considerable spatial variability in the radiative kernel.



484

485

Figure 8 The monthly average of gridded-based surface cloud radiative kernels (GCF-CRKs)

486

487

488

489

490

491

492

493

By September, the cloud radiative kernel diminishes to approximately $-0.4 \text{ Wm}^{-2}\%^{-1}$. This reduction is due to the substantial decrease in the incoming solar radiation, which in turn, lessens the absolute impact of the changes in the cloud parameters. Nevertheless, throughout the time series, there is a noticeable trend of increasing absolute GCF-CRK, particularly during the summer months, with a growth rate of approximately $0.03 \text{ Wm}^{-2}\%^{-1}$ per decade. This indicates that the influence of the CF on the surface shortwave radiation is gradually increasing.

The magnitude of the GCF-CRKs primarily depends on the intensity of the incoming SW radiation at the TOA that is reflected, absorbed, and/or scattered by clouds. To further understand



494 the factors influencing the changes in the surface SW GCF-CRNs, we analyzed the temporal and
495 spatial correlation coefficients between the GCF-CRNs and cloud parameters such as the CF, TAU,
496 cloud top/bottom pressure (CTP/CBP), and cloud top/bottom temperature (CTT/CBT). These
497 coefficients measure the strength and direction of the linear relationship between the cloud
498 parameters and the kernels (Table 1).

499 Table 1 reveals the occurrence of significant temporal and spatial variabilities in how the
500 different cloud parameters impact the surface GCF-CRNs. Across the entire Arctic region, the CBT
501 plays a dominant role in influencing the kernels. From April to September, the CBT initially
502 increases and then decreases, mirroring the trend of the absolute value of the surface GCF-CRNs.
503 This correlation is particularly strong in the oceanic regions, with a coefficient of 0.5278, which is
504 significantly higher than the correlations with the other cloud parameters (Figure A6). This suggests
505 that the magnitude of the surface GCF-CRNs decreases slightly with increasing height. The positive
506 correlation between the kernels and CTP further supports this conclusion, indicating that as the
507 height increases and the CTP decreases, the magnitude of the surface GCF-CRNs also decreases.
508 This is because less of the SW flux reaches the surface due to minimal atmospheric absorption in the
509 cloud-free layers below the clouds.

510 The next most influential cloud parameter for the surface GCF-CRNs is the TAU, as thicker
511 clouds scatter more solar radiation back into space. Over the land, the TAU's influence is
512 predominant among all of the cloud parameters, with a correlation of 0.35, which is particularly
513 noticeable in parts of North America and Asia, while there is a slight negative correlation in
514 Northern Europe (Figure A2). In the oceanic regions, this positive correlation is also evident, as the
515 range and timing of the changes in the surface GCF-CRNs' absolute value closely match those of the
516 TAU.

517 **Table 1: Temporal and spatial correlation coefficients between the cloud parameters and the surface**

518

GCF-CRNs (the absolute values are used for clarity)						
	CF	TAU	CTP	CBP	CTT	CBT
Arctic region	0.0435	0.3308	0.0275	-0.0573	0.2247	0.3396
Greenland region	-0.166	0.1536	0.03	-0.0382	0.0253	0.0203
Land no Greenland	0.0618	0.3504	-0.109	-0.0636	0.0697	0.2108
Ocean region	0.2005	0.4193	0.1867	0.0759	0.4169	0.5278

519 In Greenland, the surface GCF-CRNs are influenced by both the CF and TAU. Specifically, in
520 the northern region of the GrIS during May, June, and July, when the TAU is higher, the surface
521 GCF-CRNs' absolute value is larger in areas with lower CFs, exceeding $-2 \text{ Wm}^{-2}\%^{-1}$. In months
522 with lower TAUs, the CF slightly increases, and the corresponding surface GCF-CRNs' absolute



523 value decreases. This indicates the occurrence of positive correlations between the TAU and CTP
524 and the surface GCF-CRKs and a significant negative correlation between the CF and the surface
525 GCF-CRKs. Additionally, the changes in the CBT exhibit a significant correlation with the surface
526 GCF-CRKs in the oceanic regions.

527 **4.3 Comparison with Other Surface SW Radiative Kernels**

528 As discussed previously, most published CRK datasets are focused on the TOA. To meaningfully
529 evaluate our proposed surface CRKs, we need a surface CRK dataset that covers the Arctic region from
530 April to September for direct comparison. There is only a very limited number of such datasets that
531 satisfy the requirement and we have found only two other qualified surface CRK datasets: the
532 International Satellite Cloud Climatology Project H datasets CRK (ISCCP-FH CRK) (Zhang et al.,
533 2021) and the surface CTP/CBP CRK provided by Zhou (Zhou-CTP/CBP CRK) (Zhou et al., 2022).

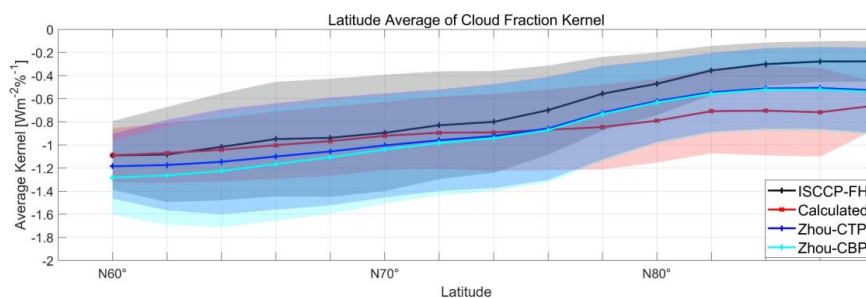
534 In their CRK calculation, the ISCCP-H data are used to produce radiative profile fluxes in 49
535 individual types of clouds for SW, long wave (LW), their sum, and net at both the TOA and surface
536 (SFC). The product only utilizes daytime observations, and the cloud types demarcated by seven cloud
537 optical depths and seven cloud effective pressure layer bins. The difference between the overcast and
538 clear sky fluxes is the overcast cloud radiative effect, and when it is divided by 100, it becomes the
539 CRK (in $\text{Wm}^{-2} \text{ \%}^{-1}$). Both the TOA and SFC CRKs are directly calculated at a 3-hour resolution on a
540 110 km equal-area map for 2007, as shown by the 49-bin histogram with the specified τ , CTP, and
541 amount of clouds. For the majority of GCM-related uses, the SFC kernel data are averaged to the
542 monthly (and annual) mean values and regridded to a 2.5° longitude \times 2.0° latitude equal-angle map.
543 This ISCCP-FH cloud radiative kernel datasets can be downloaded from
544 <https://zenodo.org/record/4677580#.YHDSaDwpCUk>.

545 The surface Zhou-CTP/CBP CRKs were constructed using the rapid radiative transfer model
546 (RRTM). The standard version of the surface CRKs is a function of the latitude, longitude, month,
547 TAU, and CBP, and the TOA CRKs depend on the latitude, longitude, month, TAU and CTP.
548 Considering that at present, the cloud property histograms created using the climate models are
549 functions of the CTP rather than the CBP, the surface CRKs on the CBP-TAU histograms were
550 converted to CTP-TAU fields using the statistical relationship between the CTP, CBP, and TAU
551 derived from collocated CloudSat and MODIS observations. These CRKs also contain seven TAU bin
552 and seven CTP bin cloud fraction histograms, which are divided according to Zelinka's cloud layer
553 classification. Additionally, they considered the ice and liquid clouds separately, so there are a total of
554 $7 \times 7 \times 2$ types of clouds for each latitude, longitude, and month of the year. Furthermore, the
555 Zhou-CTP/CBP CRKs have been evaluated using independent data sources, and they have a unique



556 advantage in reproducing the climatology and anomalies of cloud radiative effects. These CRKs are
557 available online at Zenodo (doi: <https://doi.org/10.5281/zenodo.4732640>).

558 Since our calculated kernels are based on grid-level data for all of the cloud layers, to compare our
559 GCF-CRKs with the ISCCP-FH CRKs and Zhou-CTP/CBP CRKs on a common basis, the two
560 comparison CRKs were mapped on 2-D global maps using the total TAU and CTP in the Arctic. Our
561 calculated CRKs were then resampled to match the spatial resolution of the 2-D ISCCP-FH and
562 Zhou-CTP/CBP CRKs. The resulting analysis involved a total of 12,960 grid cells on a 2.5° longitude
563 \times 2.0° latitude equal-angle map from April to September. To minimize the uncertainties introduced by
564 the other cloud parameters in the CF kernel, the TAU and CTP values used were consistent with those
565 from the CERES-SYN dataset used in this study.



566
567 **Figure 9. Comparison of latitudinal weighted means for the ISCCP-FH CRKs, Zhou-CTP/CBP CRKs,**
568 **and our GCF-CRKs**

569 Figure 9 shows the latitudinally weighted means of the ISCCP-FH CRKs, Zhou-CTP/CBP CRKs,
570 and the GCF-CRKs we calculated in this study. As can be seen from Figure 9, the latitudinal means of
571 all three CRKs are negative, they exhibit similar trends, and the magnitude of the kernels becomes less
572 negative from low to high latitudes. This indicates that the contribution of the clouds to the surface
573 shortwave radiation decreases with increasing latitude. This trend is primarily due to the reduction in
574 the solar shortwave radiation at higher latitudes and the presence of high-altitude ice clouds, which
575 tend to trap energy, causing a warming effect that reduces the cooling impact of clouds on the surface
576 (Ipcc, 2021).

577 In terms of the kernel's magnitude, the SFC GCF-CRKs range from $-1.09 \text{ Wm}^{-2} \%^{-1}$ to -0.66
578 $\text{Wm}^{-2} \%^{-1}$, i.e., a decrease of $0.43 \text{ Wm}^{-2} \%^{-1}$. The ISCCP-FH SFC CRKs vary from $-1.09 \text{ Wm}^{-2} \%^{-1}$ to
579 $-0.29 \text{ Wm}^{-2} \%^{-1}$, i.e., a change in magnitude of approximately $0.81 \text{ Wm}^{-2} \%^{-1}$. The Zhou-CTP CRKs
580 range from $-1.18 \text{ Wm}^{-2} \%^{-1}$ to $-0.53 \text{ Wm}^{-2} \%^{-1}$, i.e., a decrease of $0.65 \text{ Wm}^{-2} \%^{-1}$. The Zhou-CBP
581 exhibits a larger change, $0.74 \text{ Wm}^{-2} \%^{-1}$, particularly in the low-latitude regions where the Zhou-CBP
582 CRKs have more negative values.



583 However, when considering the latitude-weighted mean across the Arctic, our calculated kernels
584 closely match the ISCCP-FH SFC CRKs at lower latitudes ($<72^{\circ}\text{N}$), with a nearly zero difference. This
585 region is predominantly land, characterized by low CFs and minimal seasonal variations in the cloud
586 parameters. At higher latitudes ($>72^{\circ}\text{N}$), our calculated kernel resembles the Zhou-CTP CRKs, and the
587 difference between them increases with increasing latitude, reaching a maximum of $0.21 \text{ Wm}^{-2} \text{ \%}^{-1}$. At
588 high latitudes, the ISCCP-FH SFC CRKs have a smaller negative magnitude than the Zhou-CTP/CBP
589 CRKs and our GCF-CRKs have, and the difference between them and the other two types of kernels
590 increases with increasing latitude, ranging from approximately $0.1 \text{ Wm}^{-2} \text{ \%}^{-1}$ to $0.44 \text{ Wm}^{-2} \text{ \%}^{-1}$. This
591 difference is particularly notable in regions such as the sea ice melt zones, perennial open waters, and
592 GrIS where the spatial and temporal variations in the terrain and climate lead to significant CRK
593 discrepancies. We also analyzed the temporal uncertainties of the different CRKs. In lower latitude
594 regions, our estimated kernels exhibit the least temporal uncertainty, while in the high-latitude sea ice
595 regions, the temporal uncertainty of our kernels is similar to those of the other types of CRKs. This is
596 largely due to the significant seasonal variations in the kernels.

597 The vertical structure of clouds plays a crucial role in radiative processes. Both the ISCCP-FH
598 SFC CRKs and Zhou-CTP/CBP CRKs consider the radiative properties of the different cloud layers in
599 their construction. To better compare the vertical performances of the various SFC CRKs, we stratified
600 the gridded cloud properties into four pressure layers (surface to 700 hPa, 700–500 hPa, 500–300 hPa,
601 and 300–50 hPa, representing low, middle-low, middle-high, and high clouds, respectively) based on
602 the CERES-SYN stratification standard.

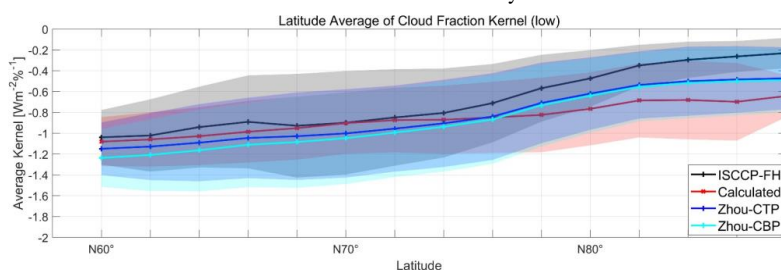
603 Figure 7 shows that for the different cloud layers, all three SFC CRKs display similar trends with
604 latitude, and the magnitude of the latitude-weighted mean decreases with increasing latitude (negative
605 values). The GCF-CRKs exhibit little sensitivity to changes in the cloud layer height as we used the
606 monthly climatological averages for each cloud layer in our calculations, which are relatively stable
607 over time. However, the ISCCP-FH SFC CRKs and Zhou-CTP/CBP CRKs exhibit some fluctuations
608 with the cloud layer height. The ISCCP-FH SFC CRKs change by approximately $0.25 \text{ Wm}^{-2} \text{ \%}^{-1}$, while
609 the Zhou-CTP/CBP CRKs change by $0.51 \text{ Wm}^{-2} \text{ \%}^{-1}$. This variation is not monotonic. For example,
610 when the cloud level rises from the low layer to the middle-low layer, the negative magnitude of the
611 Zhou-CTP/CBP CRKs increases, while it decreases when the cloud height increases continually from
612 the middle-low layer to the middle-high layer, returning to a magnitude similar to that of the low
613 clouds. Therefore, compared to the latitudinal changes, the cloud layer variations have a small impact
614 on the radiative kernel estimation.

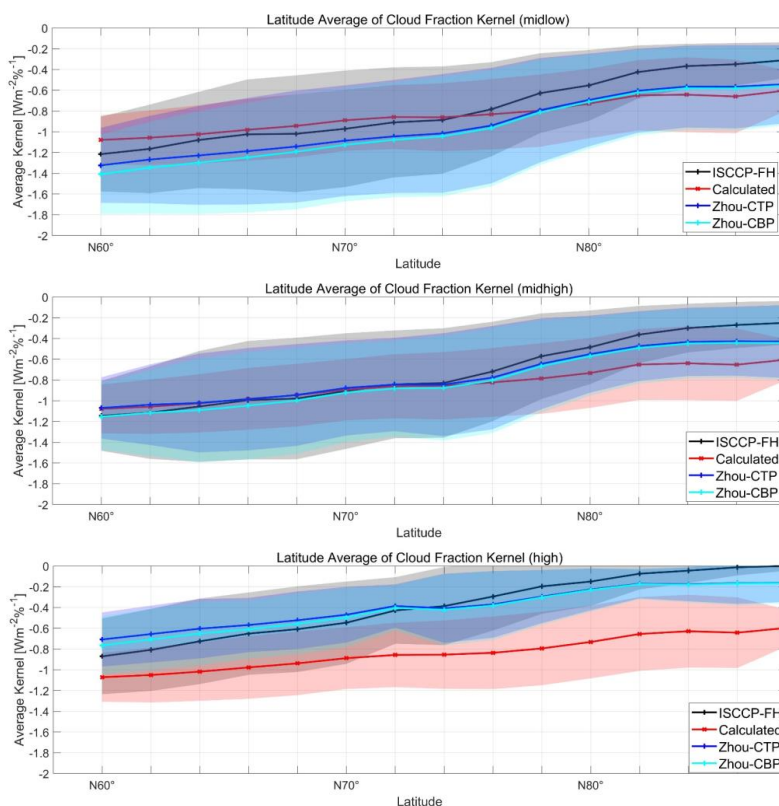
615 We observed an intriguing phenomenon: the similarity between the ISCCP-FH SFC CRKs,
616 Zhou-CTP/CBP CRKs, and GCF-CRKs varies across the different cloud layers. For example, in the



617 low level clouds, when the latitude is below 75°N, the ISCCP-FH SFC CRKs align closely with our
618 GCF-CRKs, while the Zhou-CTP/CBP CRK deviate by approximately 0.05–0.12 $\text{Wm}^{-2} \text{ \%}^{-1}$. For the
619 middle-low level clouds, the ISCCP-FH SFC CRKs are only slightly different from our GCF-CRKs in
620 the low-latitude regions, whereas the discrepancies between our kernels and the Zhou-estimated kernels
621 are 0.1–0.2 $\text{Wm}^{-2} \text{ \%}^{-1}$. However, at higher latitudes (>78°N), the difference between our calculated
622 kernels and the Zhou-CTP/CBP CRKs becomes less than 0.01 $\text{Wm}^{-2} \text{ \%}^{-1}$, indicating that even with a
623 100% CF discrepancy, the resulting radiative deviation is approximately 1 Wm^{-2} . As the cloud layer
624 continues to rise to the middle-high level, our calculated kernels again closely match the Zhou-CTP
625 CRKs at latitudes below 76°N. These findings suggest that there is significant uncertainty in both the
626 Zhou-CTP/CBP CRKs and the ISCCP-FH SFC CRKs across the different cloud layers.

627 When examining high level clouds, the differences between the GCF-CRKs and the other cloud
628 radiative kernels become most pronounced. In the Arctic, the high clouds are predominantly thin cirrus
629 clouds, and the extremely low temperatures and frequent surface inversions increase the error in
630 identifying high cirrus clouds across the different sensors (Liu et al., 2022). The vertical cloud structure
631 in the ISCCP-FH SFC CRKs is based on a combination of rawinsonde climatology and CloudSat-
632 cloud-aerosol lidar and infrared pathfinder satellite observations (CALIPSO) climatology, while the
633 statistical relationships between the CTP, CBP, and TAU in the Zhou-CTP/CBP CRKs are derived
634 from collocated MODIS-CloudSat climatology. The CRKs in our study primarily consider the cloud
635 properties from CERES-SYN1deg, which are mainly observed using the MODIS sensor. The
636 observational characteristics of these sensors contribute to the estimation errors of radiative kernels.
637 However, it is important to note that the Arctic is dominated by low clouds, which account for 50–60%
638 of the total cloud cover, while high clouds account for only approximately 3%. Therefore, the impact of
639 high clouds on the overall cloud radiative kernels is relatively small.





640 **Figure 10. Comparison of latitudinally weighted means for the ISCCP-FH CRKs, Zhou-CTP/CBP**
 641 **CRK,s and GCF-CRKs in the different cloud layers**

642 The differences between the ISCCP-FH SFC CRKs, Zhou-CTP/CBP CRKs, and GCF-CRKs
 643 exhibit significant spatiotemporal heterogeneity. In the sea ice regions, the GCF-CRKs have a larger
 644 magnitude than the other kernels (with negative differences) have, whereas the opposite is true for the
 645 land and perennial open water regions. However, Greenland is an exception where our results indicate
 646 that the CF has a more pronounced cooling effect on the surface shortwave radiation. This can be
 647 attributed to Greenland's year-round ice and snow cover, high altitudes, extreme dryness and cold,
 648 strong near-surface static stability, and persistent low-level inversion layers, which prolong the cloud
 649 duration and thus have a greater impact on the DSSR. Temporally, during the months of April and
 650 September, when the solar insolation is relatively low, the differences between these radiative kernels
 651 are smaller. However, during the months with higher solar insolation, the ISCCP-FH SFC CRKs and
 652 Zhou-CTP/CBP CRKs have larger magnitudes than our calculated CRKs have, with differences
 653 ranging from 0.3 to 0.5 $\text{Wm}^{-2}\%^{-1}$ (positive values).

654 In summary, the overall trend shows that the ISCCP-FH SFC CRKs and Zhou-CTP/CBP CRKs
 655 have latitudinal variation patterns similar to that of our calculated CRKs in the Arctic region, and the



656 differences between the various radiative kernels are much smaller than the latitudinal differences
657 within each CRK dataset. This demonstrates that latitude is a key factor influencing the surface cloud
658 radiative kernels. From a spatiotemporal distribution perspective, our calculated CRKs are generally
659 less negative than the ISCCP-FH SFC CRKs and Zhou-CTP/CBP CRKs in the land regions and more
660 negative in the ocean regions. However, in Greenland, GCF-CRKs consistently have the largest
661 magnitude (in negative terms), indicating that the cloud cover has a stronger cooling effect in this
662 region. For the different cloud layers, the various radiative kernels compared here have a high
663 consistency with our calculated kernels in specific cloud layers, demonstrating the stability of our
664 proposed kernels. As we cannot definitively determine which of the four datasets represents the
665 absolute truth, we treat them as ensemble realizations of the actual climate, and their differences serve
666 as an estimate of the uncertainty in their measurements or datasets (Zhang et al., 2006). A more
667 accurate validation would require more precise experiments, which are beyond the scope of this study.

668 4.4 Cloud Shortwave Radiative Effects in the Arctic

669 The interaction between the clouds and surface radiative parameters, known as the CRE, directly
670 impacts the radiation budget of the atmosphere-surface system and the associated temperature changes.
671 This interaction plays a critical role in regulating the annual onset of snowmelt and the yearly melting
672 and formation of sea ice in the Arctic. The surface CRE is defined as the difference in the surface
673 radiative flux under cloudy and clear-sky conditions (Cess and Potter, 1987). Accurately quantifying the
674 variations in the surface CRE in the Arctic is of paramount scientific importance for correctly
675 understanding and predicting global warming trends.

676 The role of clouds in the Arctic SW budget varies throughout the year due to the highly seasonal
677 variability of the surface albedo and atmospheric conditions. To more accurately quantify the cloud
678 radiative influences, we utilized the GCF-CRKs, combined with CF products derived from
679 multi-source satellite data, to estimate the daytime CRE in the Arctic. Additionally, we quantified the
680 surface radiative flux anomalies caused by changes in the CF. The surface CRE can be calculated using
681 the following equation:

$$682 \quad F_{CRE,swc} = \sum_i f_i \overline{K_{\Delta f, i}}, \quad (23)$$

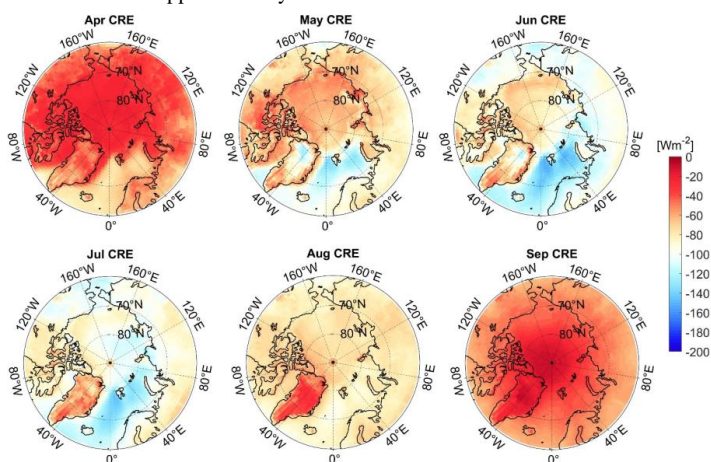
683 where $\overline{K_{\Delta f, i}}$ is the climatological monthly mean GCF-CRKs for the i th grid cell, and f_i is the
684 corresponding CF within that grid cell.

685 Figure 11 illustrates the estimated CRE averaged from April to September. As shown in Figure
686 11, the CRE is consistently negative across the Arctic during the entire study period, confirming the
687 cooling effect of the clouds in this region. This finding is consistent with the conclusions of Sledd et al.,
688 who demonstrated through satellite observations that compared to clear-sky conditions, clouds reduce



689 the average solar absorption over the land and ocean, thereby delaying the increasing trend of the
690 surface solar absorption under all-sky conditions by 20–40% (Sledd and L'ecuyer, 2021). Due to the
691 high latitudes of the Arctic region, the seasonal variation in the solar elevation angle is significant,
692 leading to considerable differences in the intensity of the surface shortwave radiation across the seasons.
693 Consequently, the CRE exhibits pronounced seasonal variability (Sedlar et al., 2010). In months with
694 lower solar insolation, such as April and September, the CRE values are relatively low, with monthly
695 averages of 42.12 Wm^{-2} and 43.87 Wm^{-2} (both negative), respectively (latitudinally weighted averages).
696 However, during the months of June and July, when the solar insolation is stronger, the monthly
697 average CRE increases to approximately 95 Wm^{-2} (negative), indicating that the clouds have a stronger
698 cooling effect on the Arctic surface during summer.

699 In terms of the spatial distribution, it was found that in addition to the solar zenith angle, the
700 surface albedo is a crucial factor influencing the surface SW CRE. In perennial open water regions, in
701 which the surface albedo is lower than that of sea ice-covered and land areas at the same latitude, the
702 surface SW CRE remains most strongly negative throughout the entire study period. This effect is
703 particularly pronounced in summer, in which the CRE exceeds 144 Wm^{-2} (negative). Conversely, the
704 surface albedo over the Greenland Ice Sheet remains high year-round, resulting in smaller shortwave
705 cloud radiative effect values, a feature that becomes even more prominent in August and September, in
706 which the value decreases to approximately -20 Wm^{-2} .



707
708

Figure 11. Climatological monthly mean Arctic CRE

709 The surface SW CRE is influenced by several cloud parameters, such as the CF, TAU, CTP, and
710 CTT. In perennial open water areas, the CF remains high throughout the year (>80%), with an annual
711 variation of approximately 5%. However, during the summer months (June–August), the TAU, CTP,



712 and CBP increase, and both the CTT and CBT are strongly correlated with the intensification of the
713 negative CRE trend.

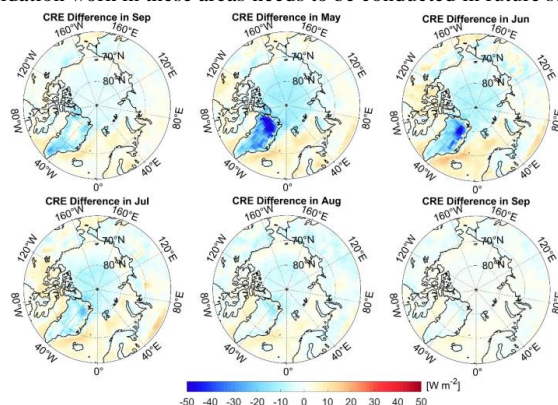
714 In the central Arctic Ocean, the CF exhibits interannual variability of greater than 30%, and the
715 CRE initially increases and then decreases over the course of the year. This trend is regulated not only
716 by the solar elevation angle and surface albedo but also by the TAU, CTP, and CTT. As the duration
717 and angle of the solar insolation increase, the Arctic sea ice melts more extensively. Studies have
718 reported that for every 106 km² reduction in the sea ice area, the annual average absorbed solar
719 radiation in the region above 75–90°N increases by 2.5 W m⁻² to 6 W m⁻² (Hartmann and Ceppi,
720 2016). This is primarily due to the positive surface albedo feedback induced by the substantial sea ice
721 changes, which further amplifies the absorption of solar radiation. However, the melting sea ice, along
722 with the intensified atmospheric and oceanic circulation, brings more warm and moist air into the
723 Arctic, enhancing cyclonic activity. This results in increased cloudiness, thicker cloud layers, and lower
724 cloud heights (Figures A1–A6). The presence of clouds can introduce a negative cloud optical
725 thickness feedback, thereby reducing the absorption of solar radiation (Goosse et al., 2018).

726 This study also compared the CRE estimated using the CRKs with the actual surface CRE
727 calculated from the CERES-EBAF, the after is derived from the differences between the all-sky DSSR
728 and clear-sky DSSR. The two CRE values had highly consistency, with a spatial correlation of 0.84, an
729 RMSE of 12.22 Wm⁻², and a bias of 1.93 Wm⁻², which suggest that the surface CRKs can effectively
730 explain the spatial distribution of the surface SW CRE observed in the Arctic. The difference
731 distribution map (Figure 12) reveals that across most of the regions of the Arctic, the error between the
732 CRE estimated using the GCF-CRKs and that estimated using the CERES-EBAF data is within 5
733 Wm⁻², particularly over land areas, excluding Greenland. However, in Greenland, the CRE intensity
734 estimated using the GCF-CRKs is significantly higher (more negative) than the CRE derived from the
735 CERES-EBAF data. This discrepancy is primarily due to the higher CF in this region, in which our
736 single-layer cloud radiative transfer model yields a higher DSSR value, resulting in more negative
737 GCF-CRKs. This effect is especially pronounced during months with stronger solar insolation (May to
738 July). Based on the accuracy validation conducted earlier using ground station data, we have reason to
739 believe that the original CERES-EBAF data underestimate the sensitivity of the DSSR to the CF in
740 Greenland.

741 Additionally, we observed that in the open ocean regions, the CRE estimated using the
742 GCF-CRKs is slightly lower than the CRE derived from the CERES-EBAF data. This is mainly
743 associated with the middle and low level clouds. When large amounts of optically thick middle and low
744 level clouds are present, they can reflect more incoming solar radiation, thereby reducing the DSSR



745 that reaches the surface. However, due to the limited observational data available for the oceanic
746 regions, further validation work in these areas needs to be conducted in future studies.

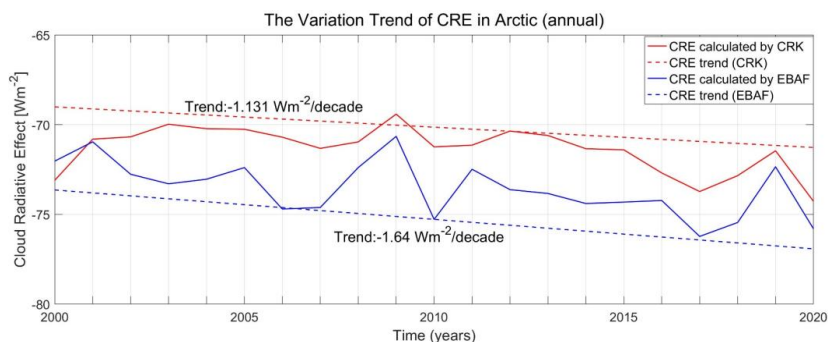


747

748 **Figure 12. Spatiotemporal distribution for the surface SW CRE differences. The CRE calculated from**
749 **the GCF-CRKs minus the CRE derived from the CERES-EBAF DSSR data.**

750 To obtain detailed information about the temporal variation in the surface CRE in the Arctic, we
751 employed the Sen–Mann–Kendall trend analysis method to calculate the long-term trends. This method
752 has been widely used in climatology for evaluating changes in climate parameters as it is more robust
753 against individual noise than the least squares method, making it more suitable for analyzing long-term
754 trends (Cai and Yu, 2009; Karlsson and Devasthale, 2018). We calculated the annual latitude-weighted
755 average CRE for both the CRE calculated using the GCF-CRK (red in Figure 13) and the CRE
756 calculated using the CERES-EBAF data (blue in Figure 13) from April to September and assessed the
757 21-year trend at the 95% significance level. The trend analysis clearly shows that the interannual
758 variations in the CRE obtained using both methods exhibit a decreasing trend (negative), indicating that
759 the cloud-induced surface radiative flux anomalies in the Arctic are increasing year by year. However,
760 the magnitude of this influence differs slightly between the two methods. The CRE calculated using the
761 CERES-EBAF data exhibits a trend of -1.64 Wm^{-2} per decade, while the trend of the CRE calculated
762 using the GCF-CRKs is gentler, -1.131 Wm^{-2} per decade. This suggests that the rate of change in the
763 clouds' influence on the surface radiative fluxes over time may not be as large as previously thought.

764 We also observed that the CRE calculated using the GCF-CRKs generally exhibits smaller
765 negative values than the CRE calculated using the CERES-EBAF data. This discrepancy is primarily
766 due to the detection of a lower CF in the perennial open water areas and many land areas, resulting in
767 higher DSSR values and a greater surface SW CRE. The largest difference between the two
768 (approximately 4 Wm^{-2}) occurred in 2010, and the smallest difference (0.15 Wm^{-2}) occurred in 2000.



769

770

Figure 13. Interannual variation trend of the cloud radiative effect (CRE) in the Arctic region (focusing only on daytime, April to September, at the 95% confidence level).

771

772

773

774

775

776

777

778

779

780

781

In terms of the spatial distribution trends (Figure A7), the overall trend patterns of the CRE calculated using the GCF-CRKs and CERES-EBAF data are consistent. Significant decreasing trends occur in the oceanic regions, while significant increasing trends occur over Baffin Island and parts of the Asian continent. The remaining regions do not exhibit significant trends at the 95% confidence level. We also noticed that in areas with significant trend changes, the CRE calculated using the GCF-CRKs exhibits a much more gradual change than that calculated using the CERES-EBAF data, suggesting that the cooling effect of the clouds on the Arctic DSSR may be overestimated. To achieve the goal of limiting the temperature rise to within 1.5°C above pre-industrial levels, more robust emission reduction measures are necessary to mitigate the impact of the Arctic amplification effect on the surface radiative energy balance.

782

5 Discussion

783

784

785

During the estimation process, there are some certainties that can impact the results. These uncertainties arise from the establishment of the radiative transfer model and the spatiotemporal sensitivity of the radiative kernels, which will be analyzed further in the following sections.

786

5.1 Uncertainty Due to Surface Albedo

787

788

789

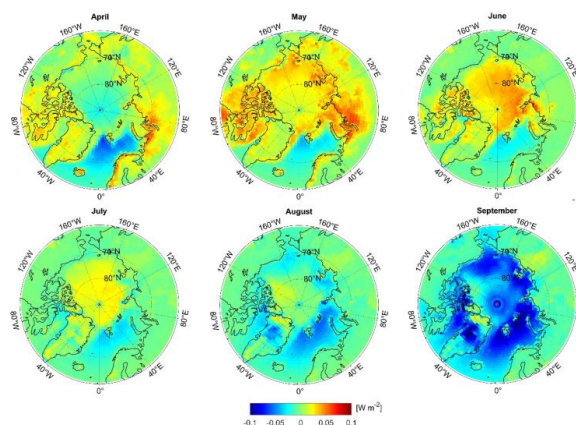
790

791

792

793

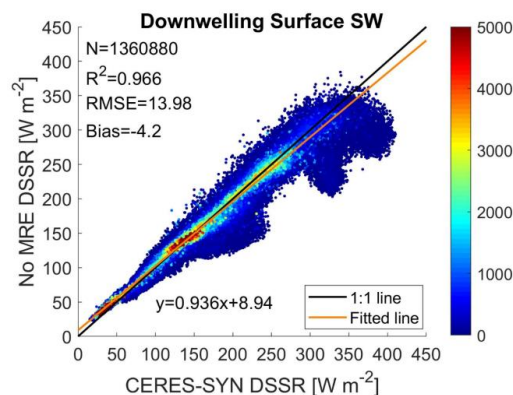
The surface albedo, defined as the ratio of the solar radiation reflected from the Earth's surface to the solar radiation incident upon it, is a crucial parameter influencing the accuracy of DSSR estimation from TOA observations. The land surface albedo is highly variable both spatially and temporally, making accurate surface albedo data essential for better characterizing the DSSR. In this study, we used the ratio of the outgoing to incident shortwave radiation under clear sky conditions as the surface albedo for the Arctic region. To assess the reliability of this albedo information, we compared it with albedo data from the CERES-EBAF dataset.



794

795 **Figure 14. Difference between the surface albedo estimated using clear sky radiation parameters and the**
 796 **CERES-EBAF surface albedo.**

797 Figure 14 presents a comparison of the spatiotemporal distributions of the albedo derived using
 798 the clear sky radiation parameters and the CERES-EBAF albedo data for the Arctic region. The
 799 difference between these two albedo estimates is generally less than 0.1. However, this difference can
 800 vary significantly with time and region. In areas with low DSSR values (e.g., open ocean in April and
 801 Arctic marine regions in September where the CERES-EBAF DSSR is less than 100 Wm²), the albedo
 802 estimated using the clear sky radiation parameters exhibits slight overestimation (approximately 3–6
 803 Wm²). This overestimation is due to the higher albedo values calculated during months with lower
 804 solar elevation angles, particularly in the oceanic regions. Conversely, in the regions with high DSSR
 805 values (where the CERES-EBAF DSSR is greater than 250 Wm²), the estimated albedo exhibits slight
 806 underestimation. This discrepancy arises because the surface albedo computed under clear sky
 807 conditions is lower than the all-sky albedo during high radiation periods, such as in May to July.



808

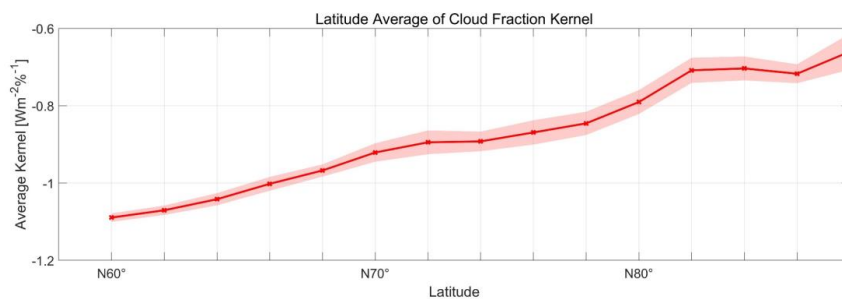
809 **Figure 15 Scatter plot comparing the DSSR estimated without considering multiple reflection effects (MRE)**
 810 **and the CERES-SYN1deg DSSR.**



811 In the Arctic region, extensive snow and sea ice cover result in high surface albedo values.
812 Research conducted by Nansen (Nansen, 2011) and subsequent studies have demonstrated that a high
813 surface albedo increases the DSSR flux under cloudy conditions (Colman, 2015; Huang et al., 2018; Li
814 Yanxing, 2022). This increase in the DSSR is attributed to multiple reflections between the atmosphere
815 (especially clouds) and the highly reflective snow/ice surface. In this study, the DSSR was divided into
816 two components: one representing the DSSR without surface contributions and another accounting for
817 multiple reflections between the surface and the atmosphere. In many studies, the first component is
818 often used as an approximation of the all-sky downward radiation flux (Liu et al., 2011; Boeke and
819 Taylor, 2016; He et al., 2019). Our results indicate that significant underestimation of the DSSR occurs
820 when multiple reflection effects are not considered (Figure 15). Compared to the CERES-SYN data,
821 the R^2 value is 0.966, a decrease of approximately 0.2; the RMSE is 4.14 Wm^{-2} higher, and the bias
822 decreases from 4.93 Wm^{-2} to -4.2 Wm^{-2} , i.e., a change of nearly 10 Wm^{-2} . This underestimation is
823 more pronounced in regions with high DSSR values, such as Greenland and sea ice areas where the
824 surface albedo is higher. Therefore, it is crucial to account for multiple reflection effects between
825 clouds and the surface when estimating surface radiation parameters in the Arctic region.

826 5.2 Temporal and Spatial Sensitivity of the Surface SW CF Radiative Kernels

827 In contrast to existing cloud radiative kernels that use radiation parameters from one year or
828 shorter periods, our study developed a long-time monthly GCF-CRK using the established radiative
829 transfer function. To better understand the temporal and spatial variability of the SFC GCF-CRK, we
830 conducted a detailed sensitivity analysis.



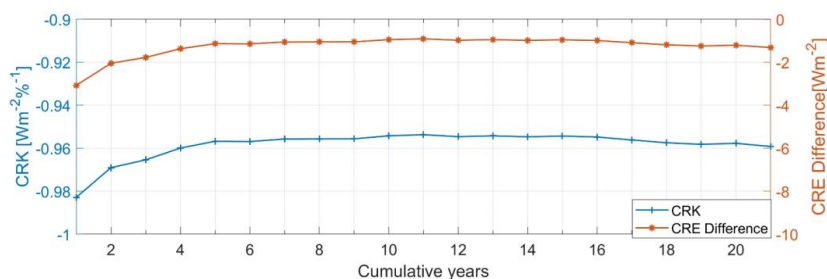
831
832 **Figure 16. Latitude-weighted mean of the deseasonalized grid-based surface cloud fraction cloud radiative**
833 **kernels (SFC GCF-CRKs)**

834 From the latitude-weighted average values of the GCF-CRKs (Figures 9 and 10) and the climate
835 monthly average distribution maps (Figure 7), it is evident that the SFC GCF-CRKs becomes less
836 negative with increasing latitude (a change of approximately $0.43 \text{ Wm}^{-2}\%^{-1}$). Additionally, there are
837 significant differences in the SW CRE calculated using the SFC GCF-CRKs across various spatial



838 locations. For example, in the sea ice areas and perennial open water regions at the same latitude, the
839 difference in the SFC GCF-CRNs ranges from approximately 0.2 to 1.2 $\text{Wm}^{-2}\%$, leading to CRE
840 deviations of greater than 50 Wm^{-2} . This highlights the significant impact of the spatial distribution on
841 the radiative kernels, suggesting that using CRNs and data for only specific regions to represent global
842 values can introduce substantial errors.

843 Furthermore, regarding the uncertainty level, the time series uncertainty within the same latitude
844 band can reach up to 1 $\text{Wm}^{-2}\%$. The regional distribution maps for different months reveal the
845 occurrence of considerable seasonal variability in the GCF-CRNs, which is closely related to the
846 seasonal changes in the solar altitude and cloud parameters. To mitigate the impact of seasonal
847 variations, we calculated the deseasonalized time series standard deviation (Figure 16). The standard
848 deviation significantly decreases across different latitude bands, although it still exhibits an increasing
849 trend with latitude. Overall, the values remain below 0.1 $\text{Wm}^{-2}\%$, indicating that seasonality is a
850 crucial factor affecting the CRNs.



851

852 **Figure 17. Differences in the grid-based surface cloud fraction radiative kernels (SFC GCF-CRNs and in**
853 **the CRE) estimated using data with varying time lengths.**

854 To further investigate the temporal sensitivity of the SFC GCF-CRNs, we calculated the SW CRE
855 using CRNs estimated over varying time periods (Figure 17). In this experiment, we calculated the
856 average SFC GCF-CRNs for 1-year to 21-year cumulative periods, with 1-year intervals, and used
857 these kernels to compute the corresponding CRE. We then compared these results with the CRE
858 obtained from the difference between the all-sky DSSR and clear-sky DSSR.

859 The analysis revealed that when using only 1 year of data to estimate the SFC GCF-CRNs, the
860 resulting CRNs are less negative than the average CRNs calculated using data for multiple years,
861 leading to a larger CRE discrepancy (approximately 2.5 Wm^{-2}). As the accumulation period increased,
862 particularly beyond 5 years, the annual average CRNs gradually stabilized, and the difference in the
863 CRE decreased (close to zero). Thus, we recommend using data spanning at least 5 years to calculate
864 the radiative kernels in order to minimize errors caused by interannual variability.



865 **6 Data Availability**

866 The gridded surface cloud fraction radiative kernels (GCF-CRKs) is available on the Zenodo
867 repository at <https://doi.org/10.5281/zenodo.13907217> (Liu et al., 2024). The data are provided in
868 netCDF format with five individual files (54.5MB) at 1° spatial resolution and monthly temporal
869 resolution only involved sunlit months from Apr to Sep during 2000-2020. The longitude ranges from
870 180°W~180°E and the latitude ranges from 60°N~90°N.

871 **7 Conclusions**

872 This paper presents a novel and more computationally efficient method for estimating the surface
873 shortwave cloud radiative effect (CRE) in the Arctic region by developing grid-based surface cloud
874 fraction cloud radiative kernels (GCF-CRKs) that incorporate spatiotemporal variability and integrate
875 refined downwelling surface shortwave radiation (DSSR) estimates and high-precision cloud fraction
876 (CF) data. The key contributions of this work are describes below.

877 **1. Enhanced DSSR Accuracy**

878 By leveraging the correlation between the top-of-atmosphere (TOA) radiative parameters and
879 incorporating the effect of cloud fraction (CF) on surface shortwave radiation under various CF
880 conditions, we derived the DSSR under all-sky conditions as a function model related to the
881 satellite-observed TOA shortwave radiation, clear-sky DSSR, and CF. By incorporating CF
882 information into the estimation process, this method addresses the limitations of traditional approaches
883 which often rely on the radiative transfer calculated under clear (CF=0) or overcast (CF=100%)
884 conditions, thus enhancing the accuracy of the DSSR estimation under partially cloudy conditions
885 ($0 < CF < 100\%$). For our Arctic-wide validation experiments using data from stations, the root mean
886 square error (RMSE) of our estimated DSSR compared to ground observations decreased by
887 approximately 1.5 Wm^{-2} , and the bias decreased by 1.23 Wm^{-2} compared to the CERES-EBAF data,
888 means an 8.7% improvement in the accuracy of the estimate. This accuracy improvement is even more
889 pronounced at the Greenland stations, with an RMSE reduction of approximately 4.53 Wm^{-2} , about
890 11.1%, and a bias reduction of approximately 6.89 Wm^{-2} .

891 **2. Development of Spatiotemporal Grid-Based CRKs**

892 To quantify cloud-induced surface radiative anomalies more accurately, we developed long-term
893 gridded surface CF radiative kernels (GCF-CRKs) based on the function model related to the CF. By
894 embedding spatiotemporal characteristics directly into the CRKs and using the observation parameters,
895 this method significantly enhances the accuracy and computational efficiency of CRE estimation in the
896 Arctic. Additionally, compared to existing methods, which decompose cloud layers and potentially
897 overlook nonlinear effects, our approach directly calculates the radiative kernels for the entire cloud
898 layer. This avoids the bias associated with the nonlinear effects in the layer-by-layer algorithm.



899 Comparisons with other CRKs, including ISCCP-FH SFC CRKs and Zhou-CTP/CBP CRKs, reveal
900 that all of the kernels have negative values with consistent spatiotemporal trends, and the magnitude
901 can be regulated by the cloud optical depth (TAU) and cloud base pressure (CBP). The results confirm
902 that our estimated kernels have better stability and increase the cooling effect of the CF in Greenland
903 by approximately $0.5 \text{ Wm}^{-2} \text{ \%}^{-1}$.

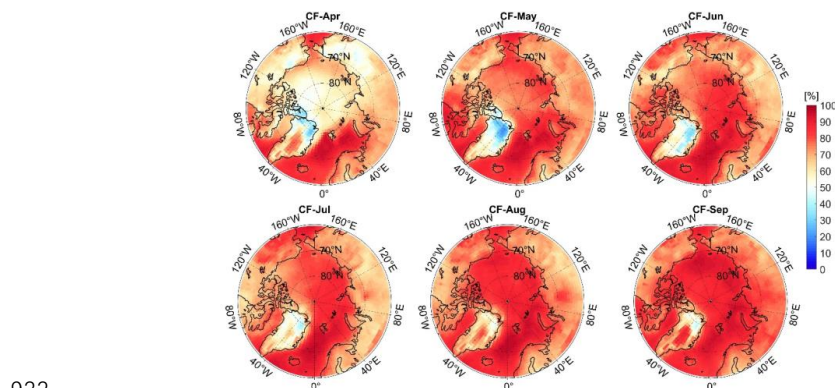
904 **3. Improved CRE Estimation**

905 By applying the developed GCF-CRKs and integrating high-precision CF data, this study provides
906 a more accurate estimation of the CRE on the Arctic DSSR. We compared these estimates with the
907 surface SW CRE calculated directly from the difference between the all-sky DSSR and clear-sky
908 DSSR in the CERES-EBAF data. The results indicate that the CRE is generally negative in the Arctic,
909 and its intensity is strongly regulated by the solar radiation intensity, surface albedo, and cloud
910 parameters (e.g., the CF, TAU, CTP, and CTT). The spatial distribution of the CRE calculated using
911 the GCF-CRKs is consistent with the CRE obtained using the CERES-EBAF data, but there are
912 important distinctions. The original CERES-EBAF data tend to underestimate the sensitivity of the CF
913 in Greenland and overestimate it in perennial open waters and some land areas due to overestimation of
914 the CF. Furthermore, Sen–Mann–Kendall trend analysis of the long-term data revealed that the surface
915 SW CRE exhibits an increasing trend in the Arctic, suggesting that previous studies may have
916 overestimated the cooling effect of clouds on Arctic surface shortwave radiation by $0.15\text{--}4 \text{ Wm}^{-2}$ and
917 overestimated the cooling rate by 0.5 Wm^{-2} pre decade.

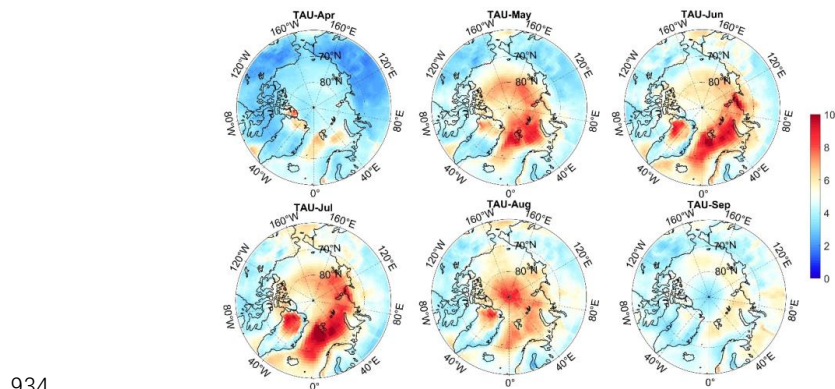
918 In summary, this study successfully demonstrates the development of a more computationally
919 efficient and accurate method for the estimating surface shortwave CRE in the Arctic by integrating
920 high-precision CF data and improved DSSR estimates into spatiotemporal grid-based CRKs. The
921 proposed approach provides significant advancements in our understanding of cloud radiative effects in
922 the Arctic and provides a robust tool for improving climate model predictions and informing climate
923 change mitigation strategies. This finding underscores the need for more robust mitigation strategies to
924 address the impact of Arctic amplification on the surface radiation energy balance. It also highlights the
925 need for continued research to refine the accuracy of radiative kernel methods, particularly in regions
926 with complex cloud dynamics and significant seasonal variability. We found that neglecting spatial
927 differences, seasonal variations, and interannual changes can result in significant temporal and spatial
928 errors. Nonetheless, this study has limitations, including the coarse spatial and temporal resolution of
929 the data and insufficient validation in marine areas. Addressing these limitations will be a focus of
930 future research efforts.



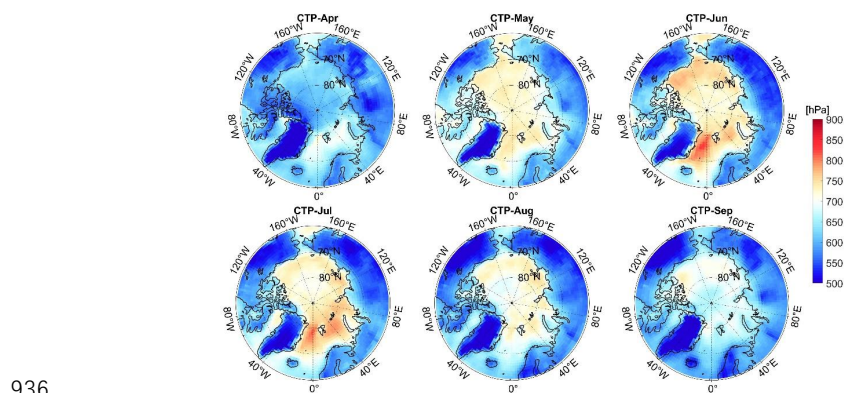
931 **Appendix A. The spatiotemporal distribution of cloud parameters**



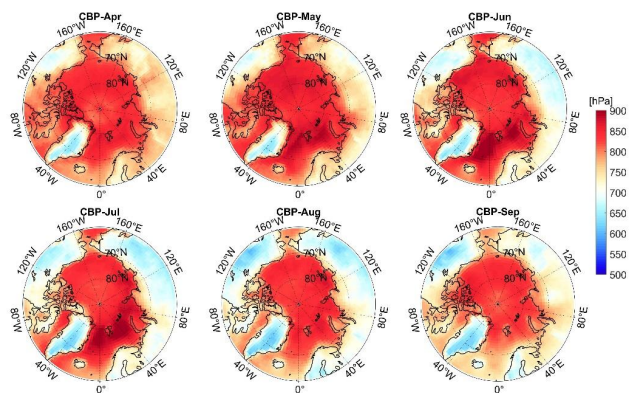
933 Figure A1. The average monthly cloud fraction (CF) in the Arctic from April to September, 2000-2020



935 Figure A2. The average monthly cloud optical depth (TAU) in the Arctic from April to September, 2000-2020

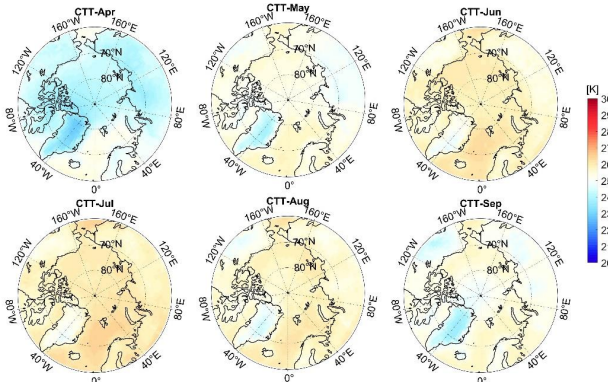


937 Figure A3. The average monthly cloud top pressure (CTP) in the Arctic from April to September, 2000-2020



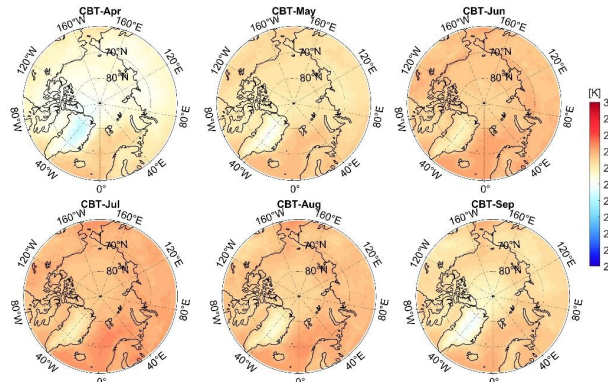
938

939 Figure A4. The average monthly cloud base pressure (CBP) in the Arctic from April to September, 2000-2020



940

941 Figure A5. The average monthly cloud top temperature (CTT) in the Arctic from April to September, 2000-2020



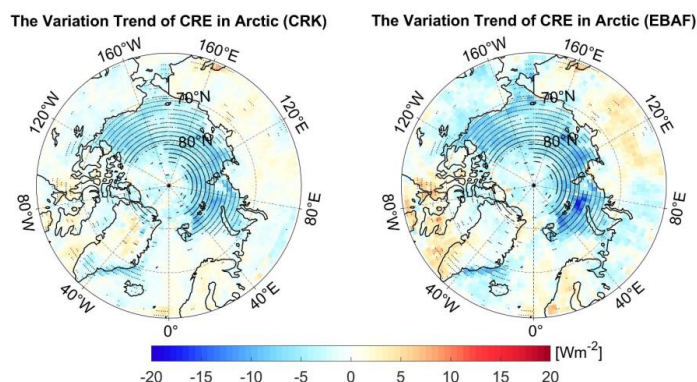
942

943 Figure A6. The average monthly cloud base temperature (CBT) in the Arctic from April to September, 2000-2020

944



945 **Appendix B. The trend distribution of the shortwave cloud radiative effect**



946

947 Figure B1. The trend distribution of the shortwave cloud radiative effect (CRE) in the Arctic. The left figure is the
948 CRE estimated by grid-specific surface cloud fraction (CF) radiative kernels and CF, and the right figure
949 represents the CRE estimated by CERES-EBAF Downwelling surface shortwave radiation differences under
950 all-sky and clear-sky. The black area shows significance at the 95% confidence level.

951 **Author contributions**

952 Xinyan Liu: Conceptualization, Data curation, Methodology, Writing - original draft,
953 Investigation, Visualization, Funding acquisition.

954 Tao He: Conceptualization, Methodology, Writing - review & editing, Supervision, Funding
955 acquisition.

956 Qingxin Wang and Xiongxin Xiao: Methodology, Writing - review & editing.

957 Yanyan Wang and Shanjun Luo: Data curation.

958 Yichuan Ma, Lei Du and Zhaocong Wu: Writing - review & editing.

959 **Competing interests**

960 The contact author has declared that none of the authors has any competing interests.

961 **Disclaimer**

962 Publisher's note: Copernicus Publications remains neutral with regard to jurisdictional claims in
963 published maps and institutional affiliations.



964 **Acknowledgments**

965 We thank the relevant teams and organizations for providing the data sets used in this study. The
966 data used for this paper have been provided by the NASA Langley Research Center Atmospheric
967 Science Data Center (ASDC). The ground data was provided by the Ameriflux, FluxNet, Global
968 Energy Balance Archive (GEBA) and the Programme for Monitoring of the Greenland Ice Sheet
969 (PROMICE). We appreciate Chen Zhou's [TOA and surface cloud radiative kernels calculated with
970 RRTM \(zenodo.org\)](#) and Yuanchong Zhang's [ISCCP-FH Cloud radiative kernel for TOA and surface
971 from the ISCCP-FH Flux Production code based on ISCCP-H data \(zenodo.org\)](#). We greatly
972 appreciated constructive comments from the anonymous reviewers and editorial team that helped us
973 improve our paper.

974 We also thank LetPub (www.letpub.com.cn) for its linguistic assistance during the preparation of
975 this manuscript.

976 **Financial support**

977 This work was supported by the Basic Foundation for Scientific Research of the Henan Academy
978 of Sciences (240625003); the Scientific Research Foundation of the Henan Academy of Sciences
979 (241825014); National Natural Science Foundation of China Grant (42090012); National Key Research
980 and Development Program of China (2020YFA0608704); and the Scientific Research Foundation for
981 High-End Talents of the Henan Academy of Sciences (242025005).

982 **References**

- 983 Ahlstrom, A. and team, P. p.: Programme for Monitoring of the Greenland Ice Sheet(PROMICE),
984 Geological Survey of Denmark and Greenland Bulletin, 15, 61-64, 2011.
- 985 Baek, E. H., Kim, J. H., Park, S., Kim, B. M., and Jeong, J. H.: Impact of poleward heat and moisture
986 transports on Arctic clouds and climate simulation, Atmospheric Chemistry and Physics, 20, 2953-2966,
987 10.5194/acp-20-2953-2020, 2020.
- 988 Betts, A. K. and Viterbo, P.: Land-surface, boundary layer, and cloud-field coupling over the
989 southwestern Amazon in ERA-40, Journal of Geophysical Research: Atmospheres, 110,
990 10.1029/2004jd005702, 2005.
- 991 Boeke, R. C. and Taylor, P. C.: Evaluation of the Arctic surface radiation budget in CMIP5 models,
992 Journal of Geophysical Research: Atmospheres, 121, 8525-8548, 10.1002/2016jd025099, 2016.
- 993 Boucher O, Randall DD, Artaxo P, Bretherton C, Feingold G, Forster P, Kerminen V-M, Kondo Y, L. H.,
994 Lohmann U, R., P, S. S., Sherwood S, Stevens B, and XY., Z.: Climate change 2013: the physical
995 science basis. Contribution of Working Group I to the Fifth Assessment Report of the



- 996 Intergovernmental Panel on Climate Change, Cambridge, United Kingdom and New York, NY, USA,
997 2013.
- 998 Cai, B. F. and Yu, R.: Advance and evaluation in the long time series vegetation trends research based
999 on remote sensing, *Journal of Remote Sensing*, 13, 1170-1186, 2009.
- 1000 Cess, R. D. and Potter, G. L.: Exploratory studies of cloud radiative forcing with a general circulation
1001 model, *Tellus A: Dynamic Meteorology and Oceanography*, 39, 460-473, 1987.
- 1002 Chen, J., He, T., Jiang, B., and Liang, S.: Estimation of all-sky all-wave daily net radiation at high
1003 latitudes from MODIS data, *Remote Sensing of Environment*, 245, 10.1016/j.rse.2020.111842, 2020.
- 1004 Christensen, M. W., Behrangi, A., L'ecuyer, T. S., Wood, N. B., Lebsock, M. D., and Stephens, G. L.:
1005 Arctic Observation and Reanalysis Integrated System: A New Data Product for Validation and Climate
1006 Study, *Bulletin of the American Meteorological Society*, 97, 907-916, 10.1175/bams-d-14-00273.1,
1007 2016.
- 1008 Colman, R. A.: Climate radiative feedbacks and adjustments at the Earth's surface, *Journal of*
1009 *Geophysical Research: Atmospheres*, 120, 3173-3182, 2015.
- 1010 English, J. M., Gettelman, A., and Henderson, G. R.: Arctic Radiative Fluxes: Present-Day Biases and
1011 Future Projections in CMIP5 Models, *Journal of Climate*, 28, 6019-6038, 10.1175/jcli-d-14-00801.1,
1012 2015.
- 1013 Gautier, C. and Landsfeld, M.: Surface solar radiation flux and cloud radiative forcing for the
1014 atmospheric radiation measurement (ARM) southern great plains (SGP): A satellite, surface
1015 observations, and radiative transfer model study, *Journal of the Atmospheric Sciences*, 54, 1289-1307,
1016 Doi 10.1175/1520-0469(1997)054<1289:Srsfac>2.0.Co;2, 1997.
- 1017 Goosse, H., Kay, J. E., Armour, K. C., Bodas-Salcedo, A., Chepfer, H., Docquier, D., Jonko, A.,
1018 Kushner, P. J., Lecomte, O., Massonnet, F., Park, H.-S., Pithan, F., Svensson, G., and Vancoppenolle,
1019 M.: Quantifying climate feedbacks in polar regions, *Nature Communications*, 9,
1020 10.1038/s41467-018-04173-0, 2018.
- 1021 Hahn, C. J., Rossow, W. B., and Warren, S. G.: ISCCP cloud properties associated with standard cloud
1022 types identified in individual surface observations, *Journal of Climate*, 14, 11-28, Doi
1023 10.1175/1520-0442(2001)014<0011:Icpaws>2.0.Co;2, 2001.
- 1024 Hakuba, M. Z., Folini, D., Wild, M., Long, C. N., Schaepman-Strub, G., and Stephens, G. L.: Cloud
1025 effects on atmospheric solar absorption in light of most recent surface and satellite measurements, *AIP*
1026 *Conference Proceedings*, 1810, 10.1063/1.4975543, 2017.
- 1027 Hartmann, D. L. and Ceppi, P.: Clouds and the Atmospheric Circulation Response to Warming, *Journal*
1028 *of Climate*, 29, 783-799, 10.1175/jcli-d-15-0394.1, 2016.
- 1029 He, M., Hu, Y., Chen, N., Wang, D., Huang, J., and Stammes, K.: High cloud coverage over melted
1030 areas dominates the impact of clouds on the albedo feedback in the Arctic, *Sci Rep*, 9, 9529,
1031 10.1038/s41598-019-44155-w, 2019.
- 1032 Huang, G., Liang, S., Lu, N., Ma, M., and Wang, D.: Toward a Broadband Parameterization Scheme for
1033 Estimating Surface Solar Irradiance: Development and Preliminary Results on MODIS Products,



- 1034 Journal of Geophysical Research: Atmospheres, 123, 12,180-112,193, 10.1029/2018jd028905, 2018.
- 1035 Huang, Y. Y., Dong, X. Q., Xi, B. K., Dolinar, E. K., Stanfield, R. E., and Qiu, S. Y.: Quantifying the
1036 Uncertainties of Reanalyzed Arctic Cloud and Radiation Properties Using Satellite Surface
1037 Observations, *Journal of Climate*, 30, 8007-8029, 10.1175/Jcli-D-16-0722.1, 2017.
- 1038 Inamdar, A. K. and Guillevic, P. C.: Net Surface Shortwave Radiation from GOES Imagery-Product
1039 Evaluation Using Ground-Based Measurements from SURFRAD, *Remote Sensing*, 7, 10788-10814,
1040 10.3390/rs70810788, 2015.
- 1041 IPCC: Climate Change 2021: The Physical Science Basis. , Cambridge University Press, Cambridge,
1042 United Kingdom and New York, NY, USA, 10.1017/9781009157896, 2021.
- 1043 IPCC: Climate Change 2022: Impacts, Adaptation, and Vulnerability, Cambridge University, United
1044 Kingdom and New York, NY, USA, 3056pp, doi:10.1017/9781009325844, 2022.
- 1045 Jia, A., Jiang, B., Liang, S., Zhang, X., and Ma, H.: Validation and Spatiotemporal Analysis of CERES
1046 Surface Net Radiation Product, *Remote Sensing*, 8, 10.3390/rs8020090, 2016.
- 1047 Jia, A., Liang, S., Jiang, B., Zhang, X., and Wang, G.: Comprehensive Assessment of Global Surface
1048 Net Radiation Products and Uncertainty Analysis, *Journal of Geophysical Research-Atmospheres*, 123,
1049 1970-1989, 10.1002/2017jd027903, 2018.
- 1050 Jiang, B., Zhang, Y., Liang, S., Wohlfahrt, G., Arain, A., Cescatti, A., Georgiadis, T., Jia, K., Kiely, G.,
1051 Lund, M., Montagnani, L., Magliulo, V., Serrano Ortiz, P., Oechel, W., Vaccari, F. P., Yao, Y., and
1052 Zhang, X.: Empirical estimation of daytime net radiation from shortwave radiation and ancillary
1053 information, *Agricultural and Forest Meteorology*, 211, 23-36, 10.1016/j.agrformet.2015.05.003, 2015.
- 1054 Karlsson, K.-G. and Devasthale, A.: Inter-Comparison and Evaluation of the Four Longest
1055 Satellite-Derived Cloud Climate Data Records: CLARA-A2, ESA Cloud CCI V3, ISCCP-HGM, and
1056 PATMOS-x, *Remote Sensing*, 10, 10.3390/rs10101567, 2018.
- 1057 Kato, S., Loeb, N. G., Rutan, D. A., Rose, F. G., Sun-Mack, S., Miller, W. F., and Chen, Y.: Uncertainty
1058 Estimate of Surface Irradiances Computed with MODIS-, CALIPSO-, and CloudSat-Derived Cloud
1059 and Aerosol Properties, *Surveys in Geophysics*, 33, 395-412, 10.1007/s10712-012-9179-x, 2012.
- 1060 Kato, S., Rose, F. G., Rutan, D. A., Thorsen, T. J., Loeb, N. G., Doelling, D. R., Huang, X. L., Smith, W.
1061 L., Su, W. Y., and Ham, S. H.: Surface Irradiances of Edition 4.0 Clouds and the Earth's Radiant Energy
1062 System (CERES) Energy Balanced and Filled (EBAF) Data Product, *Journal of Climate*, 31,
1063 4501-4527, 10.1175/Jcli-D-17-0523.1, 2018.
- 1064 Kato, S., Rose, F. G., Sun-Mack, S., Miller, W. F., Chen, Y., Rutan, D. A., Stephens, G. L., Loeb, N. G.,
1065 Minnis, P., Wielicki, B. A., Winker, D. M., Charlock, T. P., Stackhouse, P. W., Xu, K.-M., and Collins,
1066 W. D.: Improvements of top-of-atmosphere and surface irradiance computations with CALIPSO-
1067 CloudSat-, and MODIS-derived cloud and aerosol properties, *Journal of Geophysical Research*, 116,
1068 10.1029/2011jd016050, 2011.
- 1069 Kay, J. E. and L'Ecuyer, T.: Observational constraints on Arctic Ocean clouds and radiative fluxes
1070 during the early 21st century, *Journal of Geophysical Research: Atmospheres*, 118, 7219-7236,
1071 10.1002/jgrd.50489, 2013.



- 1072 Kim, D. and Ramanathan, V.: Solar radiation budget and radiative forcing due to aerosols and clouds,
1073 *Journal of Geophysical Research*, 113, 10.1029/2007jd008434, 2008.
- 1074 Kramer, R. J., Matus, A. V., Soden, B. J., and L'Ecuyer, T. S.: Observation-Based Radiative Kernels
1075 From CloudSat CALIPSO, *Journal of Geophysical Research: Atmospheres*, 124, 5431-5444,
1076 10.1029/2018JD029021, 2019.
- 1077 Letu, H., Yang, K., Nakajima, T. Y., Ishimoto, H., Nagao, T. M., Riedi, J., Baran, A. J., Ma, R., Wang,
1078 T., Shang, H., Khatri, P., Chen, L., Shi, C., and Shi, J.: High-resolution retrieval of cloud microphysical
1079 properties and surface solar radiation using Himawari-8/AHI next-generation geostationary satellite,
1080 *Remote Sensing of Environment*, 239, 10.1016/j.rse.2019.111583, 2020.
- 1081 Li Yanxing, C. L., Zhang Chunling: Spatial distribution of cloud attributes in spring and its influence
1082 on Arctic sea ice decline, *Chinese Journal of Polar Research*, 34, 177-188, 10.13679/j.jdyj.20210006,
1083 2022.
- 1084 Liu, X.: Arctic Gridded surface cloud fraction radiative kernels (GCF-CRKs) [Data set].
1085 <https://doi.org/10.5281/zenodo.13907217>, 2024.
- 1086 Liu, X., He, T., Sun, L., Xiao, X., Liang, S., and Li, S.: Analysis of Daytime Cloud Fraction
1087 Spatiotemporal Variation over the Arctic from 2000 to 2019 from Multiple Satellite Products, *Journal*
1088 *of Climate*, 35, 3995-4023, 10.1175/jcli-d-22-0007.1, 2022.
- 1089 Liu, X., He, T., Liang, S., Li, R., Xiao, X., Ma, R., and Ma, Y.: A monthly 1° resolution dataset of
1090 daytime cloud fraction over the Arctic during 2000–2020 based on multiple satellite products, *Earth*
1091 *System Science Data*, 15, 3641-3671, 10.5194/essd-15-3641-2023, 2023.
- 1092 Liu, Y., Wu, W., Jensen, M. P., and Toto, T.: Relationship between cloud radiative forcing, cloud
1093 fraction and cloud albedo, and new surface-based approach for determining cloud albedo, *Atmospheric*
1094 *Chemistry and Physics*, 11, 7155-7170, 10.5194/acp-11-7155-2011, 2011.
- 1095 Liu, Y., Ackerman, S. A., Maddux, B. C., Key, J. R., and Frey, R. A.: Errors in Cloud Detection over
1096 the Arctic Using a Satellite Imager and Implications for Observing Feedback Mechanisms, *Journal of*
1097 *Climate*, 23, 1894-1907, 10.1175/2009jcli3386.1, 2010.
- 1098 Loeb, N., Thorsen, T., Norris, J., Wang, H., and Su, W.: Changes in Earth's Energy Budget during and
1099 after the "Pause" in Global Warming: An Observational Perspective, *Climate*, 6, 10.3390/cli6030062,
1100 2018a.
- 1101 Loeb, N. G., Wang, H., Rose, F. G., Kato, S., Smith, W. L., Jr., and Sun-Mack, S.: Decomposing
1102 Shortwave Top-of-Atmosphere and Surface Radiative Flux Variations in Terms of Surface and
1103 Atmospheric Contributions, *Journal of Climate*, 32, 5003-5019, 10.1175/jcli-d-18-0826.1, 2019.
- 1104 Loeb, N. G., Doelling, D. R., Wang, H., Su, W., Nguyen, C., Corbett, J. G., Liang, L., Mitrescu, C.,
1105 Rose, F. G., and Kato, S.: Clouds and the Earth's Radiant Energy System (CERES) Energy Balanced
1106 and Filled (EBAF) Top-of-Atmosphere (TOA) Edition-4.0 Data Product, *Journal of Climate*, 31,
1107 895-918, 10.1175/jcli-d-17-0208.1, 2018b.
- 1108 Matus, A. V. and L'Ecuyer, T. S.: The role of cloud phase in Earth's radiation budget, *Journal of*
1109 *Geophysical Research: Atmospheres*, 122, 2559-2578, 10.1002/2016jd025951, 2017.



- 1110 Nansen, F.: In Nacht und Eis, BoD–Books on Demand2011.
- 1111 Norris, J. R. and Evan, A. T.: Empirical Removal of Artifacts from the ISCCP and PATMOS-x Satellite
1112 Cloud Records, *Journal of Atmospheric and Oceanic Technology*, 32, 691-702,
1113 10.1175/Jtech-D-14-00058.1, 2015.
- 1114 Pinker, R. T., Zhang, B., and Dutton, E. G.: Do satellites detect trends in surface solar radiation?,
1115 *Science*, 308, 850-854, 10.1126/science.1103159, 2005.
- 1116 Raschke, E., Kinne, S., Rossow, W. B., Stackhouse, P. W., and Wild, M.: Comparison of Radiative
1117 Energy Flows in Observational Datasets and Climate Modeling, *Journal of Applied Meteorology and*
1118 *Climatology*, 55, 93-117, 10.1175/Jamc-D-14-0281.1, 2016.
- 1119 Roesch, A., Wild, M., Ohmura, A., Dutton, E. G., Long, C. N., and Zhang, T.: Assessment of BSRN
1120 radiation records for the computation of monthly means, *Atmospheric Measurement Techniques*, 4,
1121 339-354, 10.5194/amt-4-339-2011, 2011.
- 1122 Sedlar, J., Tjemström, M., Mauritsen, T., Shupe, M. D., Brooks, I. M., Persson, P. O. G., Birch, C. E.,
1123 Leck, C., Sirevaag, A., and Nicolaus, M.: A transitioning Arctic surface energy budget: the impacts of
1124 solar zenith angle, surface albedo and cloud radiative forcing, *Climate Dynamics*, 37, 1643-1660,
1125 10.1007/s00382-010-0937-5, 2010.
- 1126 Sledd, A. and L'Ecuyer, T.: How Much Do Clouds Mask the Impacts of Arctic Sea Ice and Snow Cover
1127 Variations? Different Perspectives from Observations and Reanalyses, *Atmosphere*, 10,
1128 10.3390/atmos10010012, 2019.
- 1129 Sledd, A. and L'Ecuyer, T. S.: Emerging Trends in Arctic Solar Absorption, *Geophys Res Lett*, 48,
1130 e2021GL095813, 10.1029/2021GL095813, 2021.
- 1131 Soden, B. J., Held, I. M., Colman, R., Shell, K. M., Kiehl, J. T., and Shields, C. A.: Quantifying
1132 Climate Feedbacks Using Radiative Kernels, *Journal of Climate*, 21, 3504-3520,
1133 10.1175/2007jcli2110.1, 2008.
- 1134 Thorsen, T. J., Kato, S., Loeb, N. G., and Rose, F. G.: Observation-Based Decomposition of Radiative
1135 Perturbations and Radiative Kernels, *J Clim*, 31, 10039-10058, 10.1175/JCLI-D-18-0045.1, 2018.
- 1136 Vial, J., Dufresne, J.-L., and Bony, S. J. C. D.: On the interpretation of inter-model spread in CMIP5
1137 climate sensitivity estimates, 41, 3339-3362, 2013.
- 1138 Walsh, J. E., Chapman, W. L., and Portis, D. H.: Arctic Cloud Fraction and Radiative Fluxes in
1139 Atmospheric Reanalyses, *Journal of Climate*, 22, 2316-2334, 10.1175/2008jcli2213.1, 2009.
- 1140 Wetherald, R. T. and Manabe, S.: CLOUD FEEDBACK PROCESSES IN A
1141 GENERAL-CIRCULATION MODEL, *Journal of the Atmospheric Sciences*, 45, 1397-1415,
1142 10.1175/1520-0469(1988)045<1397:Cfpiag>2.0.Co;2, 1988.
- 1143 Wild, M., Hakuba, M. Z., Folini, D., Dorig-Ott, P., Schar, C., Kato, S., and Long, C. N.: The cloud-free
1144 global energy balance and inferred cloud radiative effects: an assessment based on direct observations
1145 and climate models, *Clim Dyn*, 52, 4787-4812, 10.1007/s00382-018-4413-y, 2019.
- 1146 Wild, M., Ohmura, A., Schär, C., Müller, G., Folini, D., Schwarz, M., Hakuba, M. Z., and



- 1147 Sanchez-Lorenzo, A.: The Global Energy Balance Archive (GEBA) version 2017: a database for
1148 worldwide measured surface energy fluxes, *Earth System Science Data*, 9, 601-613,
1149 10.5194/essd-9-601-2017, 2017.
- 1150 Xie, Y., Liu, Y., Long, C. N., and Min, Q.: Retrievals of cloud fraction and cloud albedo from
1151 surface-based shortwave radiation measurements: A comparison of 16 year measurements, *Journal of*
1152 *Geophysical Research: Atmospheres*, 119, 8925-8940, 10.1002/2014jd021705, 2014.
- 1153 Yeo, H., Kim, M.-H., Son, S.-W., Jeong, J.-H., Yoon, J.-H., Kim, B.-M., and Kim, S.-W.: Arctic cloud
1154 properties and associated radiative effects in the three newer reanalysis datasets (ERA5, MERRA-2,
1155 JRA-55): Discrepancies and possible causes, *Atmospheric Research*, 270,
1156 10.1016/j.atmosres.2022.106080, 2022.
- 1157 Zhang, Y., Jin, Z., and Sikand, M.: The Top-of-Atmosphere, Surface and Atmospheric Cloud Radiative
1158 Kemels Based on ISCCP-H Datasets: Method and Evaluation, *Journal of Geophysical Research:*
1159 *Atmospheres*, 126, 10.1029/2021jd035053, 2021.
- 1160 Zhang, Y., Rossow, W. B., and Stackhouse Jr., P. W.: Comparison of different global information
1161 sources used in surface radiative flux calculation: Radiative properties of the near-surface atmosphere,
1162 111, <https://doi.org/10.1029/2005JD006873>, 2006.
- 1163 Zhou, C., Liu, Y., and Wang, Q.: Calculating the Climatology and Anomalies of Surface Cloud
1164 Radiative Effect Using Cloud Property Histograms and Cloud Radiative Kernels, *Advances in*
1165 *Atmospheric Sciences*, 39, 2124-2136, 10.1007/s00376-021-1166-z, 2022.
- 1166 Zib, B. J., Dong, X. Q., Xi, B. K., and Kennedy, A.: Evaluation and Intercomparison of Cloud Fraction
1167 and Radiative Fluxes in Recent Reanalyses over the Arctic Using BSRN Surface Observations, *Journal*
1168 *of Climate*, 25, 2291-2305, 10.1175/Jcli-D-11-00147.1, 2012.
- 1169